Functional network organization of the mouse cortex determined by wide-field fluorescence imaging shares some —but not all— properties revealed with simultaneous fMRI-BOLD

Hadi Vafaii[1,✉], Francesca Mandino[4], Gabriel Desrosiers-Grégoire[11,12], David O'Connor[5], Xilin Shen[4], Xinxin Ge[15], Peter Herman[4], Fahmeed Hyder[4], Xenophon Papademetris[4,9], Mallar Chakravarty[11-14], Michael C. Crair[6-8], R. Todd Constable[4,5,10], Evelyn MR. Lake[4,✉], and Luiz Pessoa[2,3,✉]

[1]Department of Physics, University of Maryland, College Park, MD, 20742, USA
[2]Department of Psychology, University of Maryland, College Park, MD, 20742, USA
[3]Department of Electrical and Computer Engineering, University of Maryland, College Park, MD, 20742, USA
[4]Department of Radiology and Biomedical Imaging, Yale School of Medicine, New Haven, CT, 06520, USA
[5]Department of Biomedical Engineering, Yale University, New Haven, CT, 06511, USA
[6]Department of Neuroscience, Yale School of Medicine, New Haven, CT, 06510, USA
[7]Kavli Institute for Neuroscience, Yale School of Medicine, New Haven, CT, 06510, USA
[8]Department of Ophthalmology and Visual Science, Yale School of Medicine, New Haven, CT, 06510, USA
[9]Department of Biomedical Engineering, Yale University, New Haven, CT, 06520, USA
[10]Department of Neurosurgery, Yale School of Medicine, New Haven, CT, 06510, USA
[11]Comp. Brain Anatomy Laboratory, Cerebral Imaging Center, Douglas Mental Health Univ. Institute, Montreal, QC, H4H 1R3, Canada
[12]Integrated Program in Neuroscience, McGill University, Montreal, QC, H3A 0G4, Canada
[13]Department of Psychiatry, McGill University, Montreal, QC, H3A 0G4, Canada
[14]Department of Biological and Biomedical Engineering, McGill University, Montreal, QC, H3A 0G4, Canada
[15]Department of Physiology, School of Medicine, University of California San Francisco, San Francisco, CA, 94143, USA

✉*Correspondence to:* vafaii@umd.edu, evelyn.lake@yale.edu, pessoa@umd.edu

Abstract

Understanding the organization of large-scale brain networks remains a central problem in neuroscience. Work in both humans and rodents shows that the brain can be decomposed in terms of several networks (e.g., "default network"). Whereas the bulk of what we know is based on the blood-oxygenation level-dependent (BOLD) signal, the relationship between BOLD and neuronal activity is complex, which poses several challenges to interpreting networks revealed by this technique. To resolve these challenges, here we employed wide-field Ca^{2+} imaging simultaneously recorded with fMRI-BOLD in a highly-sampled group of GCaMP6f-expressing mice. This allowed us to determine the relationship between networks discovered by BOLD and Ca^{2+} signals both at the group level and in individual animals. Network partition used a mixed-membership stochastic blockmodel algorithm, which allows networks to be overlapping, such that a brain region may be assigned to multiple networks with varying strengths. Here, we tested the hypothesis that functional networks of the mouse brain are organized in an overlapping manner for both BOLD and Ca^{2+} data. Our findings demonstrate that BOLD large-scale networks can be detected via Ca^{2+} signals. In addition: (1) Overlapping networks were reliably estimated at the group level via random-effects statistical analysis. (2) Functional organization was generally similar for BOLD and Ca^{2+} ; e.g., with seven networks, cosine similarity was very high in five instances (values between 0.82-0.90; max possible value of 1), moderate in one case (0.73) and different in one case (0.26). (3) We discovered overlapping network organization in both data modalities, which was quantified in multiple ways; e.g., the proportion of regions that belonged to multiple networks was 75% for BOLD and 60% for Ca^{2+} . (4) The large-scale functional organization of the mouse cortex as determined by Ca^{2+} signals is considerably more similar to that with BOLD when both signal modalities are considered in the low temporal

frequency range (0.01 to 0.5 Hz). (5) Although many similarities were observed between data modalities, finer characterization uncovered key differences related to functional hubs believed to play important roles in the integration and/or segregation of signals. In particular, the spatial distribution of membership diversity (i.e., the extent to which a region affiliates with multiple networks), differed for the two types of signals. In conclusion, Ca^{2+} mesoscale signals revealed that the mouse cortex is functionally organized in terms of large-scale networks in a manner that reflects many of the properties observed using BOLD. Despite many similarities, important differences were also uncovered, suggesting that mesoscale Ca^{2+} has a strong potential to uncover additional properties of the large-scale organization of the mouse brain.

Introduction

Understanding the organization of large-scale brain networks remains a central problem in neuroscience, both in humans [1–7] and rodents [8–19]. Work in both species shows that the brain can be decomposed in terms of several large-scale systems, such as the so-called "default network" [20, 21]. The bulk of what we know is based on the blood-oxygenation level-dependent (BOLD) contrast obtained with functional magnetic resonance imaging (fMRI). The relationship between BOLD and neuronal activity is complex [22–24], which poses several challenges to interpreting networks discovered by this technique [25–28].

To address these challenges, multi-modal imaging in mice has emerged as a promising way forward [29, 30]. In these experiments, BOLD or other hemodynamic signals are concurrently acquired with calcium-indicator (Ca^{2+}) signals [29, 31, 32]. Multi-modal studies typically focus on evaluating the correspondence between Ca^{2+} and BOLD signals [29, 32–35], and some work has compared seed-based functional connectivity across modalities [31, 36, 37]. In addition, Vanni et al. reported a coarse subdivision of the cortex into 2-3 networks [38]. Despite these efforts, the relationship between BOLD and Ca^{2+} functional networks remains poorly understood; for example, the coarse decomposition by Vanni et al. does not capture the finer subdivisions described based on BOLD signals [14, 18]. To resolve this question, here we employed wide-field Ca^{2+} imaging simultaneously recorded with fMRI-BOLD [29] (Figure 1A) in a highly-sampled group of GCaMP6f-expressing mice (10 animals, 3 sessions each, 3 runs per session; Figure 1B). This allowed us to determine the relationship between networks discovered by BOLD and Ca^{2+} signals both at the group level and in individual animals.

The correlation between BOLD and Ca^{2+} time series data is maximized when Ca^{2+} is temporally bandpassed into a slow band comparable to that of BOLD [29, 32]. For example, He et al. [34] performed simultaneous single-vessel fMRI and Ca^{2+} measurements from a local patch of cortex and found that slow (0.01 to 0.1 Hz) Ca^{2+} fluctuations were similar to BOLD fluctuations. Based on these results (see also [39], [36]), we hypothesized that BOLD and Ca^{2+} networks should be more closely matched when considering the latter in the same slow frequency range as the former. To test this prediction, we considered Ca^{2+} data in two temporal frequency bands: (i) a slow band, [0.01, 0.5] Hz, identical to BOLD; and, (ii) a complementary band, [0.5, 5.0] Hz, containing faster frequencies (Ca^{2+} data were acquired at an effective rate of 10 Hz). We refer to the two bands of Ca^{2+} signal as Ca^{2+}_{slow} and Ca^{2+}_{fast} .

Many complex networks are inherently overlapping, including biological, technological, and social ones [40] [41]. Overlapping organization is important because it helps elucidate a region's potential functional contributions to multiple brain processes. In particular, regions that are multi-functional are likely to participate in multiple networks [42–45]. Most human and rodent work assumes *disjoint* functional organization, meaning a brain region belongs to one and only one network. Although, converging evidence for overlap in human brain networks has accrued based on multiple analysis techniques (latent Dirichlet allocation [46]; mixed membership algorithms [45]; edge-centric functional connectivity [7]). Nevertheless, it is unclear whether the putative overlapping organization is driven, at least in part, by the nature of BOLD signals.

Here, we tested the hypothesis that functional networks of the mouse brain are organized in an overlapping manner. Because BOLD and Ca^{2+} data were acquired simultaneously, we were able to test this prediction for each modality, separately. To do so, we employed a Bayesian generative algorithm that estimates the *membership strength* of a given node (here, brain region of interest) to all individual networks (Figure 1E) [45, 47]. If a node is a member of a single network, the algorithm assigns maximal membership strength to that network and negligible strength to other networks. Thus, in a manner that is automatically calibrated by the data, if networks are truly (essentially) disjoint as commonly assumed, the algorithm recovers a network organization that is (essentially) disjoint. In contrast, if the data support network overlap, a subset of nodes will exhibit non-trivial membership strength to more than one network.

Finally, in addition to the predictions above, we tested additional properties of BOLD and Ca^{2+} network organization. In particular, highly functionally connected hub regions are thought to play important roles in network coordination, be important for integration and/or distribution of signals, and be potential hot spots of multi-functionality [16, 17, 48–50]. However, determining hub regions with functional data remains a challenging problem [51]. For example, the common approach of using a node's graph degree is adequate when dealing with structural networks but problematic with functional ones [50, 51]. Based on the mixed-membership framework adopted here, we propose a new characterization of a region's status as a functional hub region.

Results

Simultaneous fMRI-BOLD and wide-field Ca^{2+} imaging

We studied the functional organization of the mouse cortex by using simultaneously acquired BOLD and Ca^{2+} data [29]. Head-fixed GCaMP6f mice were placed inside an MRI scanner into which we inserted optical components for Ca^{2+} signal acquisition (Figure 1A). Ten lightly anesthetized mice (0.5% isoflurane) were scanned across 3 longitudinal sessions; each session contained 4 runs, each lasting 10 minutes (Figure 1B).

We preprocessed BOLD data using the RABIES package [53], which has been successfully applied to previous mouse [18] and rat [19] fMRI datasets. This included a simple high-pass filtering step [6] which resulted in a frequency range of 0.01 to 0.5 Hz for BOLD (acquisition rate was 1 Hz; see Methods). We considered Ca^{2+} data of two frequency bands: Ca^{2+}_{slow} exactly matching the BOLD frequency, and Ca^{2+}_{fast} which was high-pass filtered in the range between 0.5 and 5 Hz (acquisition rate was 10 Hz). Ca^{2+} data were processed using methods described previously[54].

Relating 3D BOLD and 2D Ca^{2+} imaging data within a common space

To build functional networks, a common set of regions of interest (ROIs) was defined (Figure 1C; Methods). To relate 3D BOLD and 2D Ca^{2+} data, we adopted the CCFv3 common space for the mouse brain provided by Allen Institute for Brain Sciences [52]. ROIs covered most of the cortex but left out lateral regions such as the insula and temporal association areas that were not sufficiently covered by optical imaging (Figure 1D). Correlation matrices were first computed for each *run* by determining the pairwise Pearson correlation between ROI time series data and were binarized by keeping the top $d\%$ strongest edges. We present results mainly for 512 ROIs and $d = 15\%$ but explored other values to ascertain the robustness of the results across a range of parameter choices.

Bayesian overlapping networks

We used a mixed-membership stochastic blockmodel [55] algorithm that accepts binary graphs as input and determines overlapping networks [45, 47]. The algorithm determines *membership values* for regions, one value

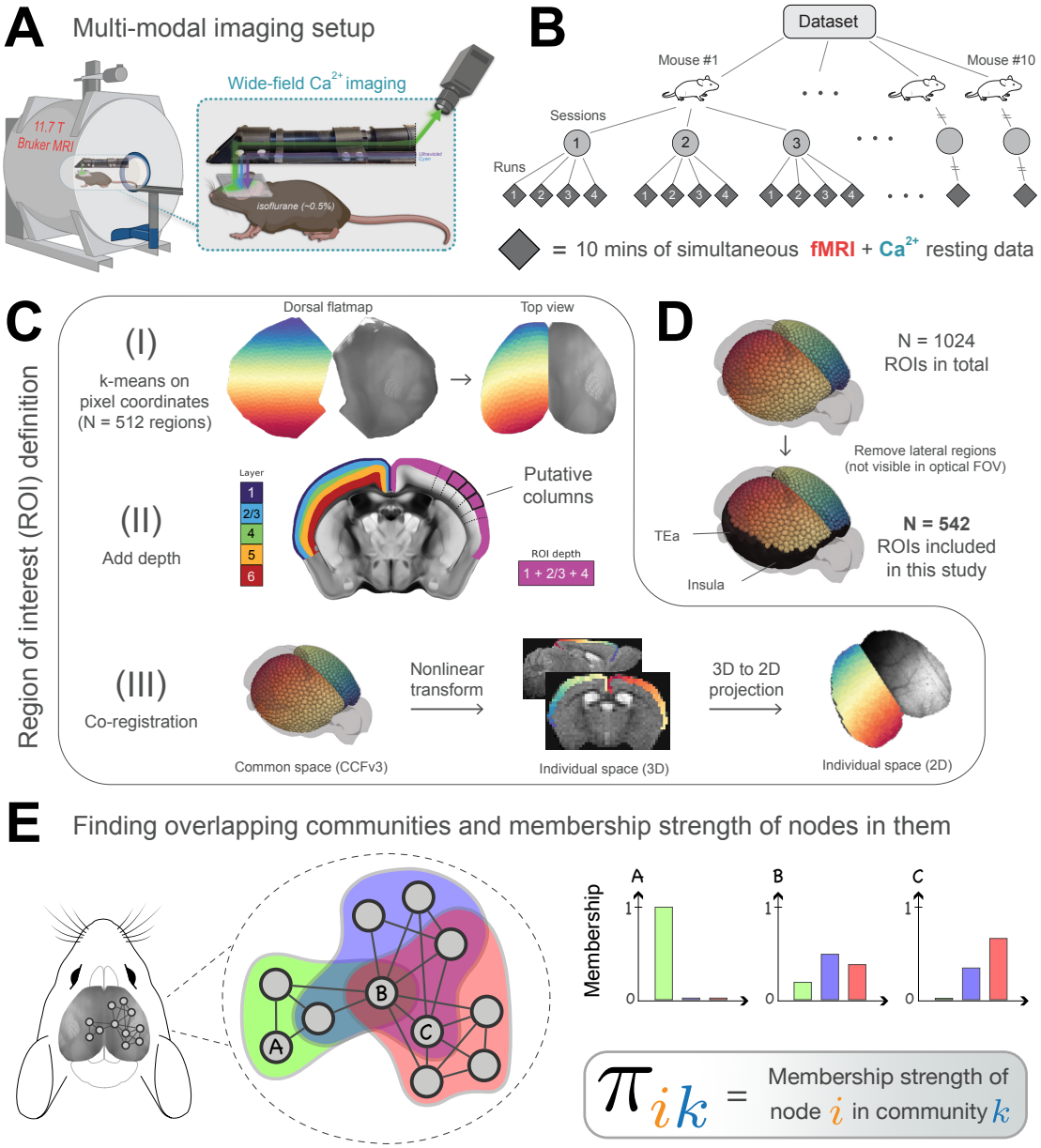

Figure 1: Experimental setup and overlapping community analysis. **(A)** Simultaneous fMRI-BOLD and wide-field Ca^{2+} imaging on lightly anesthetized GCaMP6f mice ($\sim 0.5\%$ isoflurane). **(B)** Hierarchical structure of the data. $N = 10$ mice, scanned across 3 longitudinal sessions, with 4 runs per session each lasting 10 mins, yielding a total of 120 mins of resting-state data per animal. **(C)** Defining regions of interest (ROI) within CCFv3 [52]; (I) Divide the mouse dorsal flatmap into a total of $N = 1024$ spatially homogeneous regions (left and right hemispheres are mirror symmetry); (II) Add depth by following streamlines normal to the surface of cortex at each depth. Built this way, the ROIs can be interpreted as putative cortical columns; finally (III) Transform ROIs from the common space into 3D and 2D individual spaces (see Methods). Dorsal flatmap, layer masks, and columnar streamlines are available within CCFv3. **(D)** In this study, we restrict our analysis to the subset of ROIs that appeared in the optical field of view (FOV) after co-registration. This choice allows us to compare BOLD and Ca^{2+} networks using an identical group of regions but leaves out lateral areas such as the insula or temporal association areas (TEa). **(E)** We applied a mixed-membership stochastic blockmodel algorithm [47], which accepts binary graphs as input and detects overlapping communities in them. More importantly, it also determines continuous membership values for each node in these communities. *Membership value* is a number between 0 and 1 and quantifies the affiliation strength of a node in a community. In this cartoon example, node A belongs only to the green community, whereas node B belongs to all three communities with varying strengths. We organized membership values as a matrix, π, which has a shape of $\#nodes \times \#communities$ (11×3 here), and its rows add up to 1 since membership values are normalized. π is the main product of the algorithm and our primary quantity of interest. We will work with π or its derivatives in the remainder of this paper.

for each network (Figure 1E). Suppose there are K networks. For each region (node), the algorithm determines a membership vector, namely, the strength of participation of the region with each network: a membership value, π_{ik}, indicates the membership strength of region i in network k. For example, node A in Figure 1E belongs only to the green community, while node B belongs to all three communities with varying strengths. Membership can be thought of as a limited resource, such that they sum to 1, which allows membership values to be interpreted as probabilities. Overlapping networks were computed at the level of *individual runs*. Specifically, membership values were determined for individual runs and averaged across sessions to determine an animal-level result. In this manner, we were able to estimate the variability of membership values while performing group-level statistical tests.

Overlapping network organization

To uncover network organization, we performed overlapping network detection as a function of the number of networks, across conditions. Recent work has shown decomposition of the mouse cortex into as few as 3 networks [16, 17, 38], but more typically has uncovered 7-10 networks [14, 18]. With 3 networks, our approach uncovered an organization that captured previously observed systems [16, 17], namely, the visual (OC2) and latero-frontal (OC3) networks, as well as a large system (OC1) that included cortical territories classified as the default network in other studies [21] (Figure 2A). To facilitate comparison with standard disjoint algorithms, we also determined a version of the network assignment in which brain regions were assigned the network label with the largest membership value. Our results are also in agreement with those based on Ca^{2+} seed-based correlation maps [31, 32, 37, 38, 54, 56], especially for BOLD and Ca^{2+}_{slow} . With 7 communities, well-defined visual and lateral cortical networks (OC2 and OC3, respectively) were again identified [14, 16, 18], together with additional systems covering bilateral and well-defined cortical territories (Figure 2C). We also investigated a considerably larger number of communities (total of 20) (Figure S1), revealing finer spatial networks that were mostly organized bilaterally.

Next, we quantitatively compared the results of the different conditions. We focused on the case when the cortex was subdivided into an intermediate number of networks (i.e., 7 networks). In particular, we evaluated the hypothesis that band-pass filtering Ca^{2+} signals to match that of BOLD signals leads to a Ca^{2+} network organization that more closely resembles the organization observed with BOLD. Networks were compared using cosine similarity (a score of 1 indicates identical organization, 0.5 indicates neither similar nor dissimilar organization, and 0 indicates perfectly dissimilar organization). The similarity between BOLD and Ca^{2+}_{slow} networks was relatively high, except for OC7, a community that was evident in both Ca^{2+} conditions but not captured by BOLD. In comparison, the similarity between BOLD and Ca^{2+}_{fast} communities was generally lower but still relatively high for OC1-OC4 though modest for OC5 and OC6.

Combined, these results revealed that band-pass filtering Ca^{2+} signals had the strongest impact on the OC5 and OC6 networks (Figure 2C). Notably, in both cases, Ca^{2+}_{slow} networks were very similar to the corresponding BOLD networks. BOLD OC5 captured very well a region known as the anterior lateral motor area, which is involved in motor planning [57–60]. BOLD and Ca^{2+}_{slow} OC6 were centered around the barrel cortex. For Ca^{2+}_{fast} , OC4 and OC5 overlapped with the barrel cortex. Ca^{2+}_{fast} OC6 was roughly centered around the upper-limb area.

Notably, OC7 was maximally different across modalities (Figure 2D). For BOLD, OC7 was centered around an area in the secondary motor cortex commonly referred to as the frontal orienting field, possibly related to the frontal eye field in primates [61–63]. For both Ca^{2+} conditions this area was contained within OC4 and did not appear as a separate community (this was also the case when investigating 20 communities; Figure S1). Instead, for both Ca^{2+} conditions, OC7 was centered around the retrosplenial cortex.

To further quantify the similarity between BOLD and Ca^{2+} communities, we combined all communities to provide an overall index of similarity. In particular, we tested the prediction that the similarity between BOLD

and Ca^{2+}_{slow} would be higher than that between BOLD and Ca^{2+}_{fast} [36]. Indeed, this relationship was statistically significant when the cortex was partitioned into 3, 7, and 20 overlapping networks ($p < 0.05$, permutation test, Holm–Bonferroni corrected). Importantly, these results were stable across multiple processing parameters, including thresholding of the functional connectivity matrices, and the number of regions used to subdivide cortex (Figure S4). See Figure S2 for networks found at the individual animal level.

In summary, overlapping networks can be reliably estimated from both BOLD and Ca^{2+} data. Although several properties of large-scale systems captured by BOLD were largely reproduced by Ca^{2+} data, some important differences were discovered, too, and will be further explored below. Importantly, our analysis confirmed the hypothesis that BOLD networks are more similar to those obtained with Ca^{2+} data that is band-passed to match the slow temporal frequency range considered for the former. In what follows, we focused on the overlapping community organization with 7 communities, which captures large-scale cortical systems of intermediate size, as most often investigated in the literature [14, 18].

Quantifying overlapping organization

To what degree is cortical large-scale network organization overlapping? To quantify overlapping organization, we examined the distribution of membership values across networks. Membership values range from 0 to 1, and sum to 1 across networks. Thus, from the perspective of a specific region, if it has high membership value for one of its networks, the total membership across the remaining networks will be low. In particular, a disjoint organization would be revealed as having all regions with very high membership for a single community ("peaked" membership value distribution; Figure 3A left); conversely, a closer to uniform distribution would correspond to a network whose nodes affiliate with multiple networks but with varying strengths (Figure 3A middle).

To obtain membership distributions, we divided the range [0.2, 1.0] into four bins of equal width (membership values < 0.2 were not considered). This approach was selected based on our experiments on synthetic LFR graphs with known ground truth overlap sizes [64]. Specifically, in this binning scheme disjoint graphs have all their membership values concentrated in the last bin (0.8, 1.0] (see Figure S5).

Across conditions, networks contained no more than 60% of brain regions with the highest level of membership ($>$ 0.8). In other words, approximately 40% of the regions belonged to at least 2 networks, demonstrating substantial network overlap. The least overlapping networks were the visual and lateral-frontal (for all conditions), and the retrosplenial for the two Ca^{2+} conditions (Figure 3B). Among the most overlapping networks, across all conditions, OC4 contained $\sim 60\%$ of the regions that belonged to more than one community (see also OC1). Taken together, our results demonstrate that the mouse cortex contains a substantially overlapping network structure. Such organization was present for BOLD and both Ca^{2+} frequency bands.

Cortical networks exhibited core and periphery organization

In standard disjoint networks, all regions have the same status within the network (but see Section on **network degree**). The determination of overlapping organization allowed us to evaluate the following question: what regions are part of a community's *core* or, conversely, its *periphery*? Here, we answer this question in a principled manner that takes variability across individuals into account [65, 66]. To this aim, we defined a region to *belong* to a network if its membership value for that community exceeds a given threshold value (one-sample t test, FDR corrected; see Methods).

We defined core regions as those with membership values > 0.5, that is, regions with the majority of their membership to that particular community (Figure 4). Such regions are likely of low functional diversity, such as sensorimotor areas, as can be seen in OC-2 and OC-3. However, we also found core regions in parts of the cortex that likely are more functionally diverse (see OC4-7). Regions with membership values reliably above 0.05 or 0.1

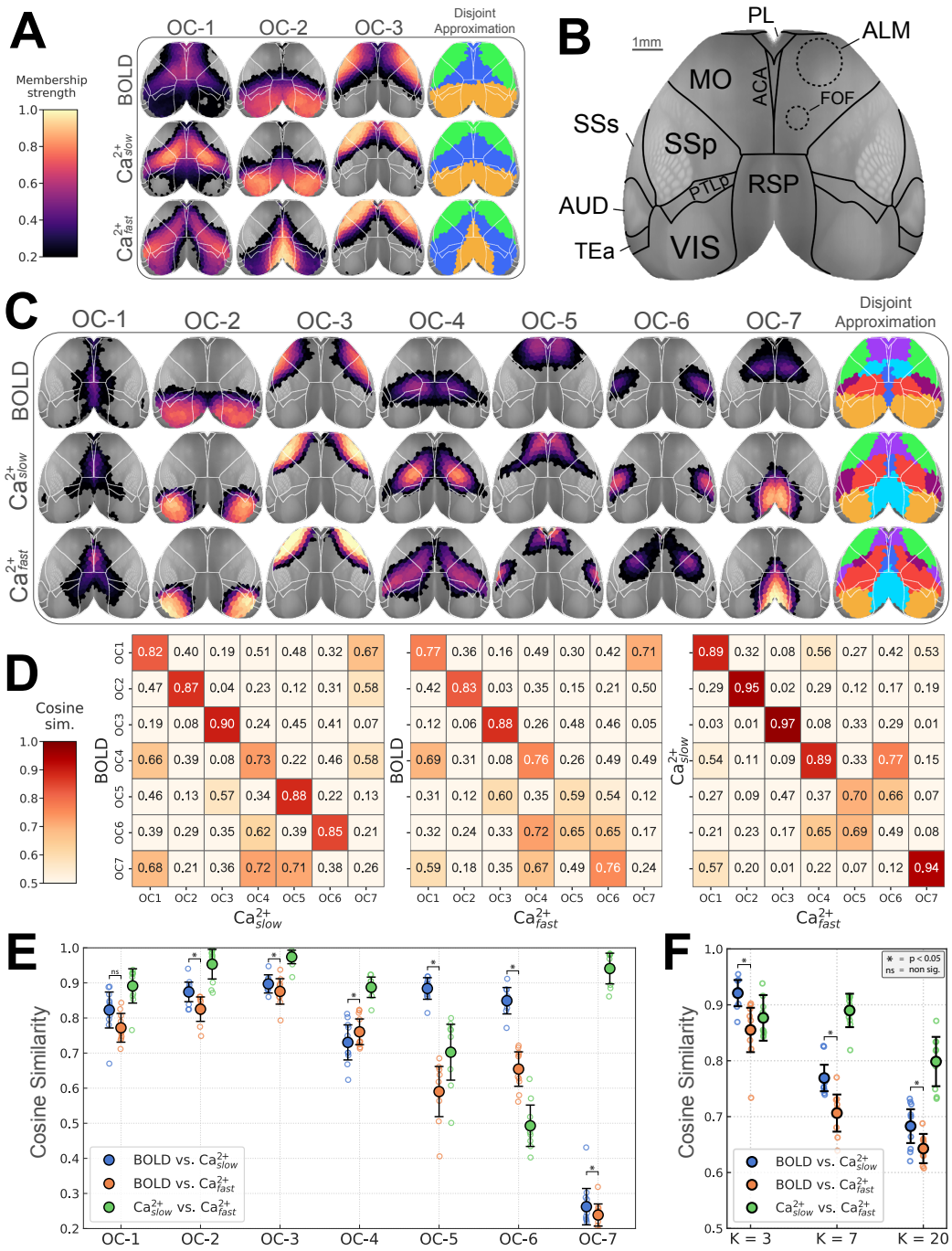

Figure 2: Overlapping functional networks of the mouse cortex. **(A)** At a coarse level, the mouse cortex is decomposed into $K = 3$ overlapping communities (OC). OC1, default-mode-like; OC2, visual; and, OC3, somatomotor networks. Color scale indicates membership strengths (see Figure 1E). The disjoint approximation is obtained by taking each node's maximum membership value. **(B)** Cortical areas visible from the top view. **(C)** $K = 7$ networks solution breaks the default network into several subnetworks. **(D)** Quantifying network similarities by computing normalized dot product of network membership vectors (i.e. cosine similarity). 1 = identical, 0.5 = neither similar nor dissimilar, 0 = perfectly dissimilar. **(E)** Diagonal elements of matrices in D are shown. $N = 10$ empty circles correspond to individual mice, large circle is the group average. **(F)** Overall similarity scores were obtained by computing the dot product of entire membership matrices. **(E-F)** BOLD networks are more similar to Ca^{2+}_{slow} than they are to Ca^{2+}_{fast}, permutation test, $p < 0.05$, Holm-Bonferroni corrected. Error margins are 95% confidence interval, hierarchical bootstrap ($N = 1,000,000$ iterations). VIS, visual areas; PTLp, posterior parietal association areas; RSP, retrosplenial area; ACA, anterior cingulate area; SSp, primary somatosensory area; SSs, supplemental somatosensory area; MO, somatomotor areas; PL, prelimbic area; FOF, frontal orienting field; ALM, anterior lateral motor cortex. See also Figure S1, Figure S2, Figure S3, and Figure S4.

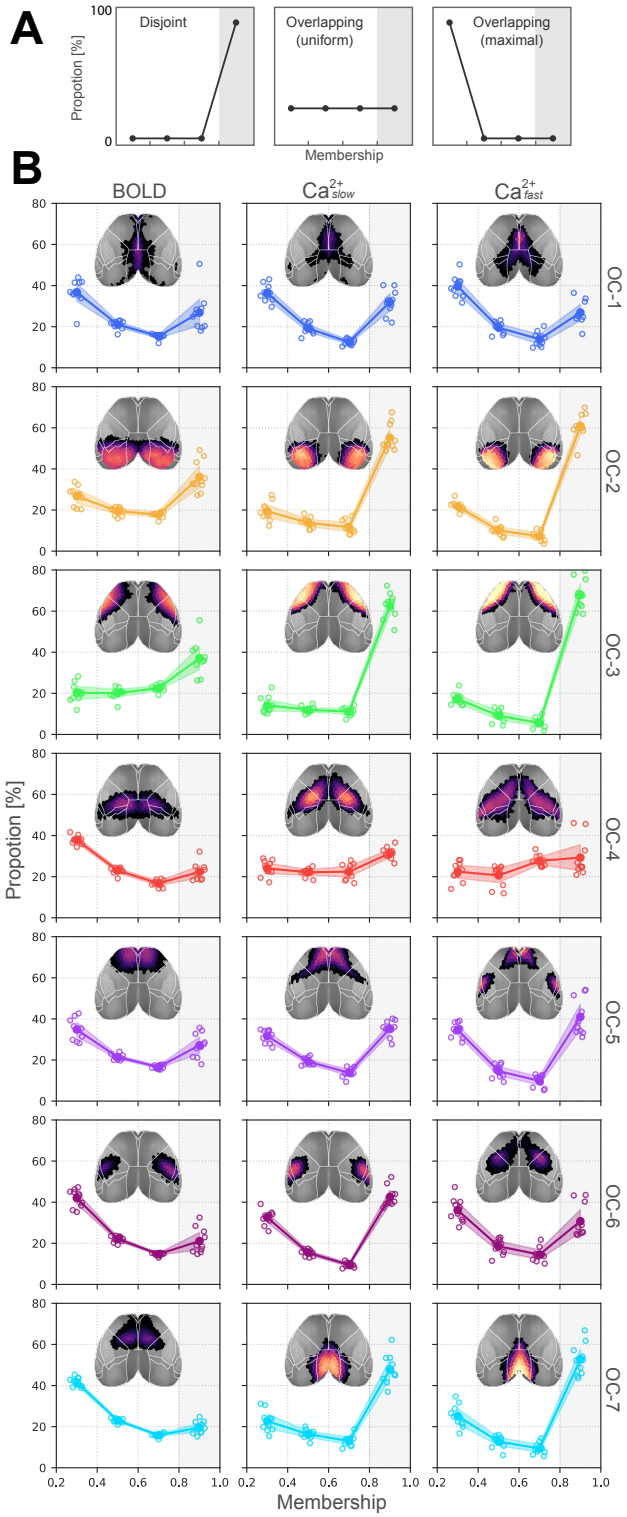

Figure 3: Distribution of membership values. **(A)** Three illustrative distributions. Left, disjoint organization with no small or mid-range memberships; Middle, overlapping with uniform weights in all membership values; Right, completely overlapping with no mid-range or stronger memberships. **(B)** Membership distributions computed from the real data hint at a substantial overlap. Note that here the y-axis is capped at 80%, indicating that none of the networks are disjoint. Compare with Figure S5.

(but not greater than 0.25) can be deemed to belong to a network's periphery. Overall, the overlapping organization is organized in a spatially coherent fashion that reveals a spatial arrangement of core and periphery network

components.

Majority of brain regions belonged to multiple communities

The approach of the previous section allows us to quantify the number of networks an individual regions belong to. Specifically, if a region exhibited a membership value reliably (i.e., statistically) greater than a specific critical value, the region was deemed as belonging to the associated network (Figure 4B). Here, we set the value as 0.1 representing the fact that at least 10% of its membership weight should be allocated to a network (naturally, the value is arbitrary and other choices could be adopted). For both BOLD and Ca^{2+} conditions, the majority of brain regions belonged to more than one network (Figure 4B and C), and a substantial number of regions belonged to 2-3 networks, with a small number belonging to 4.

Finally, to quantify the extent of network overlap at the network level, a similar approach was employed. We defined the network overlap score as the proportion of regions belonging to a network that belonged to multiple networks. We found that network overlap was very high in multiple cases (Figure 4D). For BOLD, network overlap was $> 80\%$ in all but one network. For Ca^{2+}_{slow} networks were less overlapping than for BOLD; whereas some networks were still very overlapping (85%; OC1, OC4, OC6), the overlap was more modest for OC2, OC3, and OC7. Finally, Ca^{2+}_{fast} networks were the least overlapping, although three of them still exhibited scores $> 90\%$.

In summary, the majority of cortical brain areas of the mouse belonged to at least two communities, a property observed with both BOLD and Ca^{2+} data. Simultaneously, large-scale cortical networks were highly overlapping, and even the least overlapping ones were comprised of no more than 40% of regions that were affiliated with a single network.

Membership diversity is spatially organized

The preceding analysis allowed us to estimate the extent of network overlap by utilizing a binary criterion for membership. However, such discretization discards continuous information that can be used to characterize *membership diversity*. Here, to quantify graded membership information, we computed a measure of membership diversity: A region that belongs to all communities with equal membership strength will have a maximum diversity of 1; a region that belongs to a single community will have a minimal diversity of 0. A natural way to compute such a measure in the context of probability-like values such as membership strengths is by using normalized Shannon entropy.

The distribution of membership diversity values is shown in Figure 5A. A substantial number of regions exhibited diversity values very close to zero (for example, approximately 30% for Ca^{2+}_{slow}), indicating that their membership strength was exclusively associated with one network. Excluding this peak at zero diversity, the remaining nodes displayed values more or less along a continuum. However, of the regions associating with multiple networks (i.e., non-zero diversity), a considerable number of them affiliated with two communities (dashed line; e.g., a region with membership value of 0.5 with network 1, 0.5 with network 2, and 0 with the remaining communities).

The spatial distribution of membership diversity is shown in Figure 5B, which revealed partial agreement across BOLD and the Ca^{2+} conditions, and especially strong agreement between the two Ca^{2+} frequency bands. To quantify the agreement between conditions, we computed the Pearson correlation between membership diversity values for all condition pairs. Correlation between BOLD and Ca^{2+}_{slow} was $\rho = 0.54 \pm 0.11$; between BOLD and Ca^{2+}_{fast} was $\rho = 0.63 \pm 0.09$; and between the two Ca^{2+} frequencies was $\rho = 0.90 \pm 0.07$ (variability based on bootstrapping; see Methods).

Next, we explicitly compared membership diversity maps to determine ROIs that showed differences between conditions Figure 5B. We found that membership diversity was consistently larger for BOLD compared to both

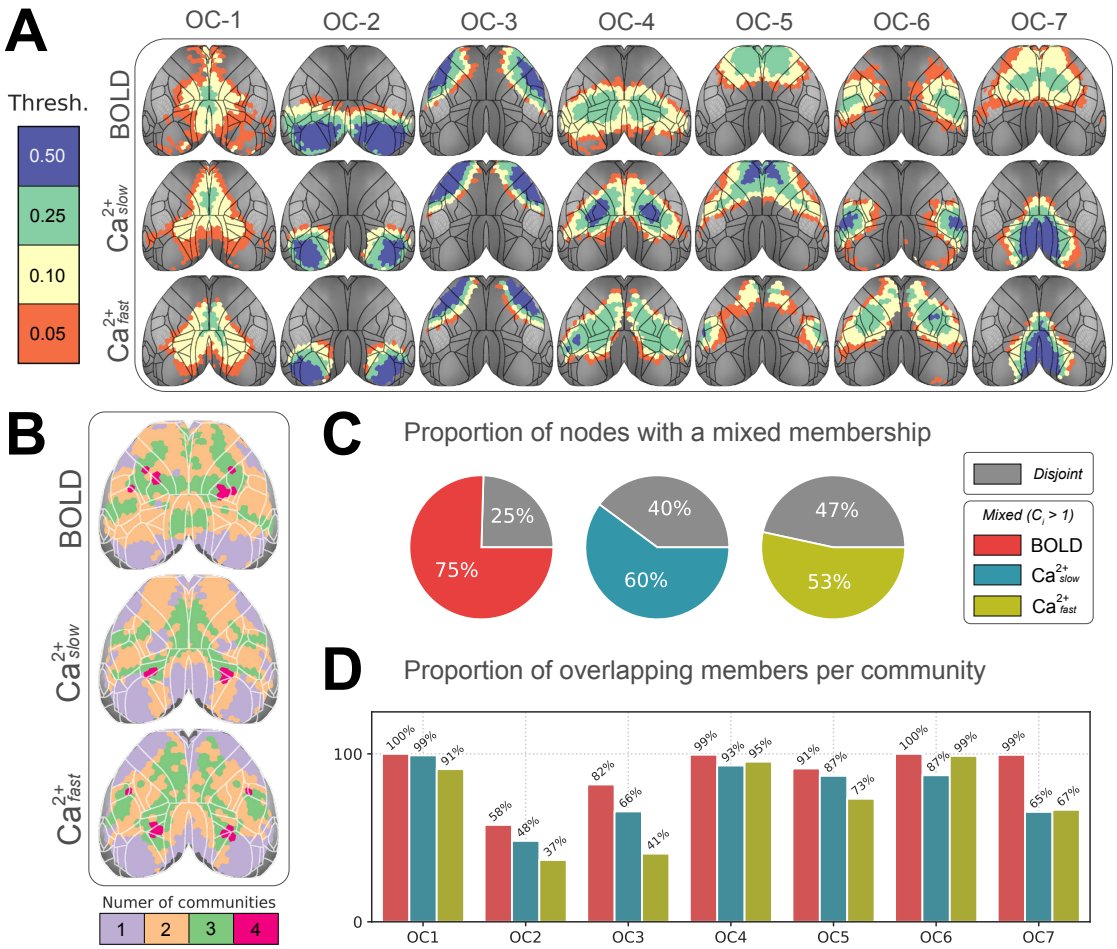

Figure 4: Quantifying overlap extent. **(A)** We used a statistical thresholding method to decide if a node *belongs* to a network or not. Members of networks are shown as a function of the threshold. Blue (strong threshold $\mu > 0.5$) reveals faithful members, whereas orange ($\mu > 0.05$) reveals the spatial extent of the network. **(B)** Using a threshold of $\mu = 0.1$, we counted number of parent networks for each node. Most regions belong to more than one network. **(C)** We defined a global *overlap score* for the entire graph as the ratio of overlapping nodes divided by the total number of nodes. For all modalities, more than half of the network is overlapping. **(D)** Overlap score at the network level is defined similarly. All networks are highly overlapping, except visual (OC2) and somatomotor (OC3) networks. A somewhat surprising finding is that for both Ca^{2+} conditions, the RSP network (OC7) is relatively less overlapping than other networks.

Ca^{2+} conditions, except for delimited sectors of the cortex. Intriguingly, Ca^{2+}_{fast} exhibited a large territory of ROIs with larger membership diversity compared to Ca^{2+}_{slow} . In summary, overlapping networks can be described in terms of the diversity of their region's affiliations. We found an intermediate amount of agreement in the spatial distribution of membership diversity across all conditions, but the highest degree between the two Ca^{2+} conditions.

High degree nodes strikingly different across data modalities

Hub regions, namely those with a high number of connections, are thought to play important roles in the integration and/or distribution of brain signals [51, 67], monkey [], cat [], and mouse brain networks [16]. Here, we determined functional hubs by computing the graph *degree* of brain regions based on BOLD and Ca^{2+} functional connectivity matrices. Are degree distributions and spatial distribution preserved across the three conditions? The distribution of degree values for BOLD was shifted toward lower values compared to Ca^{2+} , whereas the distributions for the latter were more similar to each other Figure 6A. The spatial distribution of degree also differed considerably between BOLD and Ca^{2+} conditions Figure 6C, as further quantified by the scatter plots of

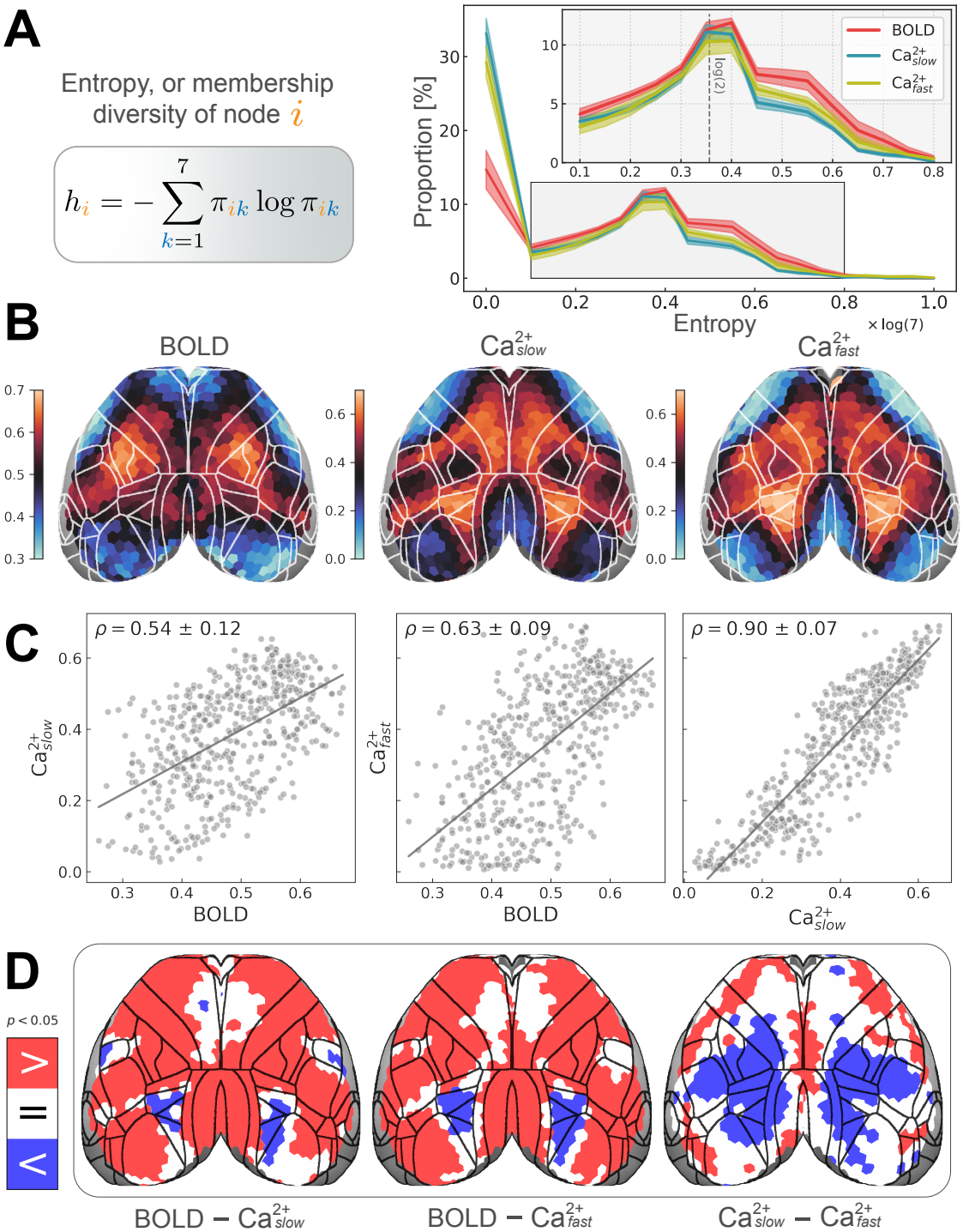

Figure 5: Introducing node entropy centrality. **(A)** Shannon entropy is applied to node membership vectors to quantify membership diversity. The values are normalized to the range $[0,1]$. If node i is disjoint (i.e. it belongs to a single network only) we would have $h_i = 0$. In contrast, $h_i = 1$ if it belongs to all networks with equal strength. Right: distribution of node entropies. The largest peak occurs at $h = 0$, corresponding to disjoint nodes. The second largest peak occurs at $h \approx \log(2)$ which corresponds to a situation where a node has a membership of 0.5 in two networks and 0 elsewhere. **(B)** Node entropies visualized on the cortex. Unimodal areas such as visual and somatomotor areas are low entropy, whereas, multi-modal regions within the DMN are high entropy. **(C)** The inferred entropy values are highly correlated across modalities. **(D)** Permutation test reveals BOLD $>$ Ca^{2+} in most regions, except for some frontal areas where BOLD $=$ Ca^{2+} , and higher visual areas where BOLD $<$ Ca^{2+} . See also Figure S6.

Figure 6C. Importantly, degree values were highly correlated between the two Ca^{2+} conditions. These differences

persisted after accounting for variability by creating percentile maps [16] (not shown).

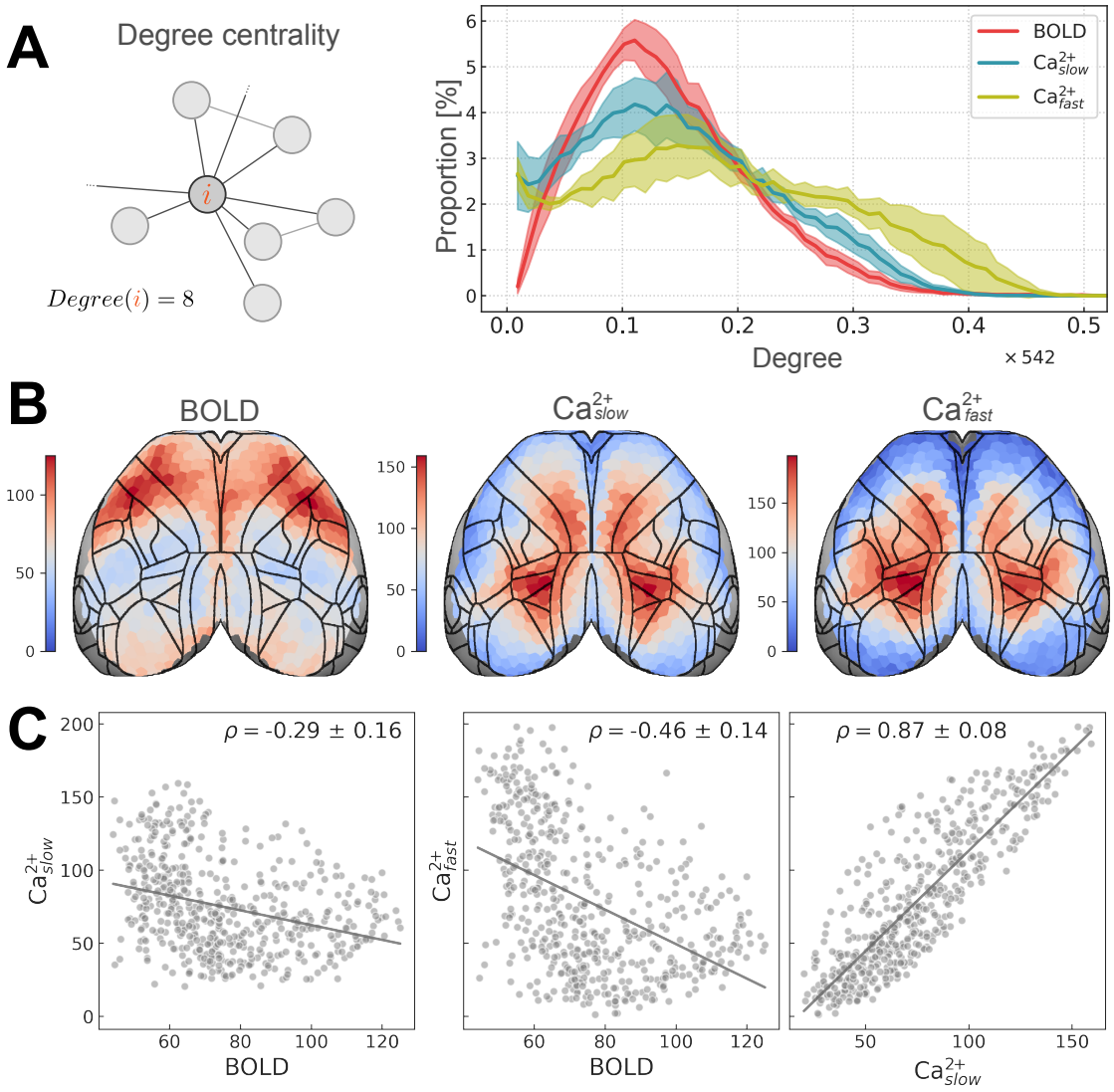

Figure 6: High degree nodes are strikingly different across modalities. **(A)** Node degree count is one of the most basic and widely used measures of network topology. Right: degree distributions are different across modalities, with BOLD being more similar to Ca^{2+}_{slow} than Ca^{2+}_{fast} . **(B)** Average node degrees visualized on the cortex, which reveals the discrepancy across modalities. **(C)** The dissimilarity is quantified by the negative correlation between BOLD and Ca^{2+} results. See also Figure S7.

Relationship between membership diversity and degree

Relatively high degree has been suggested to be an important property of nodes that affiliate with multiple communities [68]. However, in the context of overlapping networks, membership diversity provides a powerful way to index the engagement of a given region with multiple communities. Here, we compared node degree and node membership diversity across conditions (Figure 7). We found that the two measures were inversely correlated for BOLD, positively correlated for Ca^{2+}_{slow} , and more strongly correlated for Ca^{2+}_{fast} . In the scatter plots, we indicate the spatial location of regions in terms of the colored sectors of part B.

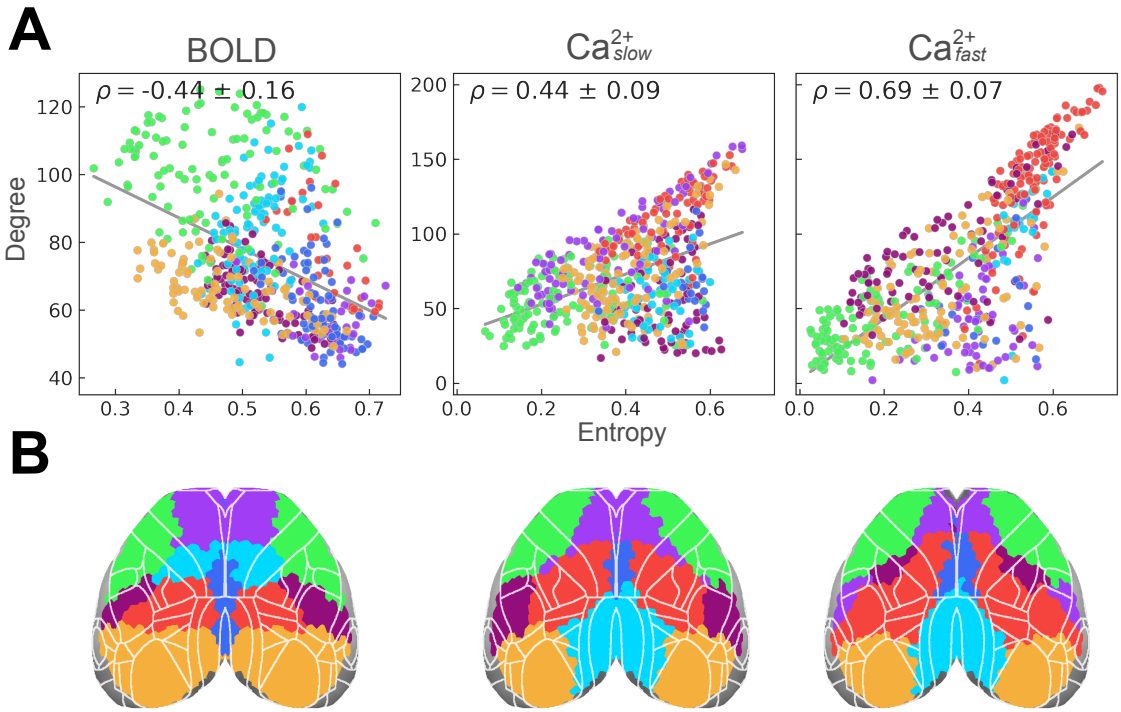

Figure 7: Functional cartography of the mouse cortex. **(A)** Entropy (a measure of connection diversity) and degree (a measure of connection strength) are plotted. We observe a negative correlation for BOLD, similar to previous reports [51]. In contrast, the relationship is positive for both Ca^{2+}_{slow} and Ca^{2+}_{fast} , with a larger correlation for Ca^{2+}_{fast} . **(B)** Nodes are colored according to their disjoint network assignment (see last column in Figure 2C). See also Figure S6.

Discussion

In summary, we used a simultaneous dataset of fMRI-BOLD and wide-field Ca^{2+} imaging to characterize the functional architecture of the mouse cortex, both at the group level (Figure 2, Figure S1, and Figure S3); and individual level (Figure S2). We compared the spatial structure of the resulting networks and found that the networks discovered by BOLD are largely reproduced by Ca^{2+} data, in a frequency-specific way: BOLD networks are more similar to Ca^{2+}_{slow} than they are to Ca^{2+}_{fast} (Figure 2D-F, Figure S3D-F, and Figure S4). Thus, temporal frequency band plays an important role in determining large-scale network organization. Despite the overall agreement across modalities, we observed important differences as well (see below).

Analyzing the resulting membership values confirmed the overlapping hypothesis: for all modalities networks are extensively overlapping. Therefore, using an overlapping framework is a necessity in mapping large-scale brain networks. Next, we used the membership vector of a node to define entropy centrality (Figure 5), which we proposed as a metric to detect hubs in functional graphs. In contrast, we found node degree to be of limited use in our functional networks, and a potentially misleading measure (Figure 6, Figure S7). Thus, using an overlapping framework is not only necessary (Figure 3, Figure 4), but also useful (Figure 5, Figure 7).

Functional networks of the mouse cortex

Large-scale networks of the mouse brain have been characterized using fMRI via seed-based or independent component analysis (ICA) [13, 14, 18, 69]. Less commonly, this question has been also explored using Ca^{2+} imaging data. For example, Vanni and colleagues reported networks in the mouse cortex in two dominant frequency modes: 3 networks found in a slow band ($< 1Hz$), and 2 networks in faster band ($\sim 3Hz$) [38]. Their networks

reproduced across a variety of clustering methods; however, they revealed only a coarse decomposition of the mouse cortex which leaves out important details that are available only if finer decompositions are explored.

Others have reported functional connectivity maps obtained from seed-based analysis in a multi-modal setting [31, 36, 37, 56]. These studies typically record concurrent GCaMP6 and hemoglobin Ca^{2+} signals to detect neuronal and hemodynamic responses, respectively. However, seed-based maps are rudimentary, and they depend on the choice of specific seeds used. Hence, they don't reveal the overall network organization. (See also [33] for k-means and [70] for group ICA network analysis).

In the present work, for the first time, we report the comprehensive network organization of the mouse cortex. A unique strength of our work is using a multi-modal dataset comprised of simultaneous fMRI-BOLD (the most popular imaging method in human studies) and Ca^{2+} imaging (a signal with neuronal specificity and high spatiotemporal resolution) which expands its translational potential [30].

In the case of $K = 3$ networks we report a coarse decomposition of the dorsal cortex into a DMN-like network (OC1), a visual network (OC2), and a latero-frontal network (OC3), which is often referred to as a possible precursor of the executive network in humans [13, 71] (Figure 2A). Our results resemble previous seed-based reports, however, they are somewhat different from the networks of Vanni et al., possibly because our mice were anesthetized while they used awake mice [38].

Increasing to $K = 7$ networks leaves the visual (OC2) and somatomotor (OC3) networks largely unchanged, while the DMN-like network breaks into several subnetworks (Figure 2C). This is reminiscent of reports that the human DMN is comprised of several smaller components [72, 73]; however, such comparisons should be taken with a caveat because clear homologs may not exist.

Similarities and differences in network structure across modalities

The spatial patterns of the networks appear similar across modalities, which we quantified using cosine similarity. Some networks are highly similar across all conditions (e.g. OC1-4), whereas other networks exhibit differences (Figure 2D-E) especially see OC7.

In certain networks such as OC5 and 6, Ca^{2+}_{slow} is more similar to BOLD than it is to Ca^{2+}_{fast} . This is remarkable, because controlling for frequency band leads to this divergence between Ca^{2+}_{slow} and Ca^{2+}_{fast} , overcoming the fact that they are the same signal, sharing the same biophysical properties. Such an increase in BOLD/Ca^{2+}_{slow} similarity relative to Ca^{2+}_{slow} /Ca^{2+}_{fast} similarity is consistent with a previous report that brain dynamics in the infraslow band is distinct from faster bands and therefore brain dynamics in different bands capture distinct neurophysiological properties [39]. This likely explains the observed divergence between Ca^{2+}_{slow} and Ca^{2+}_{fast} in OCs 5 and 6.

At the level of overall network similarity, we found that BOLD is consistently more similar to Ca^{2+}_{slow} than it is to Ca^{2+}_{fast} . This was true for all decompositions that we explored: $K = 3, 7$, and 20 networks (Figure 2F). Our findings are consistent with previous reports that hemodynamics and Ca^{2+} seed-based maps are spatially more similar in the slow band, relative to a faster band [36].

These results naturally depend on the choice of hyperparameter used, such as granularity and number of ROI, or the edge-filtering threshold. These choices are somewhat arbitrary, therefore, to ensure the robustness of our findings we repeated our study while covering a combinatorial space of analysis conditions: using both coarse and fine ROIs (see Figure S3B), with graph densities spanning the range $d = 10\% - 25\%$ in incremental steps of 5%. The results were reproduced over all of these conditions indicating the robustness of the observed patterns (Figure S4).

The overlapping organization is substantial and non-negligible

We sought to evaluate the large-scale organization of the mouse cortex. Is it overlapping, and if yes, to what extent? We tested this by analyzing the membership values using two complementary approaches as follows. First, the distribution of membership values revealed that over half of the nodes express intermediate membership strength in networks (Figure 3). To interpret this result, we applied an identical procedure to synthetic graphs with known overlap sizes. We found that in strictly disjoint networks, 100% of the nodes have strong membership values in the range $[0.8, 1.0]$ and no node has small or intermediate membership value less than 0.8 (Figure S5). This is in sharp contrast to our empirical findings (Figure 3), indicating that brain networks are far from disjoint.

Second, we used a statistical thresholding method to quantify the proportion of overlapping nodes in networks. At the global network level, the majority of nodes ($> 50\%$) belonged to multiple networks (Figure 4C). As for the individual networks, most had high overlap scores greater than 70% indicating that 70% of their members belong to at least one other network (Figure 4D). Collectively, these results support the notion that the mouse cortex is a system with a highly overlapping architecture. Given such large amounts of overlap, enforcing strict disjoint organization is not a good approximation and likely leads to an impoverished and incomplete characterization of the network organization.

Brain centrality measures and their relationship to each other

Entropy: a community-aware centrality measure

Hub regions are considered to be important integrators of information in the brain; however, identifying them using functional data has proven difficult. Hubs are typically identified by rank-ordering nodes according to graph theoretic centrality measures such as degree or betweenness [48]. However, such measures are meaningful only when applied to structural networks [48, 51]. For correlation-based functional connectivity networks, community structure and community-aware measures such as participation coefficient are shown to be more appropriate [51]. Here we proposed a more straightforward approach to achieve a similar goal: by virtue of having access to dense membership values, we were able to define a new centrality measure, entropy, which quantifies the membership diversity of regions in a continuous manner (Figure 5A). Entropy values are largely consistent with participation coefficient (Figure S6), indicating that they capture similar underlying phenomena.

Does membership diversity translate to functional diversity?

Entropy maps revealed regions of the brain that are more overlapping than others, therefore, are considered hub candidates. The observed spatial patterns agree with previous reports: unimodal regions (e.g. visual and somatomotor) have relatively smaller entropy values, whereas, multi-modal regions are high entropy, indicating that these regions belong to multiple networks (Figure 5B).

Regions in posterior-parietal cortex (PTLp) and some higher visual areas were among the highest entropy regions in both modalities. This is especially visible in Ca^{2+} data (Figure 5B, but also see Figure 4B). Studies have reported the involvement of PTLp in diverse cognitive functions such as navigation and decision making [74], which indicates multi-functionality. Therefore, in this case, high entropy hubs that belong to multiple networks are also multi-functional.

The situation is more complex for BOLD because it predicts high entropy for some unimodal somatosensory areas such as SSp-tr and SSp-ll. In contrast, Ca^{2+} data identifies these regions as low entropy islands surrounded by high entropy regions, which is more consistent with our prior expectations. Furthermore, these regions were also clustered unexpectedly as parts of the DMN as inferred using BOLD-ICA [21]. More work is needed to understand the discrepancy between BOLD and Ca^{2+} findings in this part of the somatosensory cortex.

Issues with hubness as measured by node degree

Inferred entropy values are more similar across data modalities; however, we observed qualitatively and quantitatively different degree centrality across modalities (compare Figure 5C with Figure 6C). The discrepancy was not an artifact introduced by the choice of preprocessing steps (Figure S7). Degree or entropy, which one is a better measure for detecting important hubs? Bertolero and colleagues [50] addressed a similar question by studying a large variety of networks and found that diverse clubs (nodes with diversely distributed links), rather than rich clubs (interconnected high-degree nodes), play a more prominent role in the integration of information in networks. Furthermore, studies in network science have advocated for considering community-aware centrality measures [75]. Taken together, these findings suggest that degree centrality may not be an appropriate measure for functional networks.

Relationship between degree and entropy centralities

From a network science perspective, overlapping communities are shown to reconcile two fundamental organizational principles of networks: (i) community structure; and, (ii) core/periphery structure [68]. In this view, it is proposed that the densely connected core of the network (i.e. the rich club) is where communities meet and overlap. This leads to the prediction that high degree and high entropy should be correlated across nodes. We tested this empirically and found that it is true to some extent for Ca^{2+} data, but not for BOLD Figure 7. The anti-correlation between node degree and diversity scores has been previously reported for fMRI-based human functional networks [51]. Here for the first time we test this for both BOLD and Ca^{2+} networks in mice and find a surprising divergence across modalities: BOLD is anti-correlated but Ca^{2+} is positively correlated, and this positive relationship is frequency dependent. Previous work has shown that rich clubs and diverse clubs are not necessarily the same set of nodes [50], consistent with our BOLD results but contrasting Ca^{2+} results. We conclude that the relationship between degree and entropy depends strongly on the data modality.

The entropy-degree relationship is visualized in Figure 7. We observe clustering of nodes in compact regions of this space in accordance with their disjoint community assignment. This is reminiscent of previous work that demonstrated nodes with similar functional roles occupy nearby regions of such cartographic landscapes [76]. In our data, we found that the latero-frontal network (OC3) is the least diverse network across all modalities Figure 7, green). This is anticipated because this network is comprised mostly of unimodal somatomotor regions. However, this result seemingly contradicts previous ones. For example, Liska et al. report that this network (referred to as latero-cortical network (LCN) in their work) is the most diverse cortical network [16]. The conflict can be resolved if we consider that their study was performed on the entire brain and LCN included the insula, which might contribute to the high diversity scores found in their study. In the present work, we focused only on regions that appeared in the 2D optical field of view. Hence, the insula was left out (Figure 1D). This leads to the prediction that insula is a highly overlapping brain area, which we will test in future work by considering whole-brain networks for BOLD.

Limitations

Anesthetized

It is important to note that in this study we used anesthetized mice. It has been shown that network structure is preserved under light anesthesia and awake conditions; however, important distinguishing signatures of consciousness are also reported [77]. Future work is needed to address how the overall network organization and its characteristics (such as the amount of overlap) is modified in the awake condition.

Overlap size: why BOLD > Ca^{2+} ?

All modalities show large amounts of overlap (> 50%, Figure 4C); however, BOLD is more overlapping than both Ca^{2+} conditions. Why? This could be due to processing steps used in BOLD such as spatial smoothing, or overall poor spatial resolution in BOLD data. The resulting overlap scores depend on two crucial steps: (i) inferring functional interaction graphs from data; and, (ii) applying the algorithm to the graphs and computing overlap scores. We did our best to minimize potentially inflated values via several measures. First, in this study, we used relatively sparse graphs ($d = 15\%$), which ensures only strong correlation values survive the threshold. If a processing step such as smoothing increases correlation values, it does so uniformly and probably it does not significantly alter the set of top 15% of links that survive the binarization threshold. Second, we applied all our measures at the run level, for example, proportions reported in Figure 3 and entropy values reported in Figure 5 are all calculated *per run* and then averaged over runs to get the group-level estimates. This minimizes the chances of inflated overlap scores that might be due to artifacts such as misalignment across individuals during spatial normalization. Head motion is known to systematically alter the correlation structure across brain regions [78], which could in turn alter derived overlap scores. To address this, we applied a conservative threshold to remove high motion frames inferred from BOLD data [53] (the same set of frames removed from both modalities; see Methods). Finally, we applied a statistical thresholding method to eliminate small membership values that were not significantly different than zero (see Methods). Despite all these strict measures, we still found non-negligible overlap scores for both BOLD and Ca^{2+} modalities, which suggests this phenomenon has biological roots.

Broad implications in neuroscience

Disjoint networks come with an implicit assumption that each brain region has a single function as reflected in its binary (all or none) network affiliation. This assumption has its root in functional localization, the idea that each brain region performs a single, specific function [79, 80]. However, these theories are slowly being replaced with new ones that embrace the possibility of many-to-many region-function correspondence [81, 82].

Recent experiments in behaving mice have shown that sensory and motor processing may not be cleanly segregated in the brain [83]. For example, an unexpectedly large fraction of the variance in the activity of neurons in "*sensory*" areas such as the primary visual cortex can be explained as a function of carefully monitored movement variables [84, 85]. As another example, Ebrahimi et al. [86] recorded neuronal activity throughout spatially distributed regions in the mouse cortex during visual decision making. In their data, a considerable portion of neurons in anatomically defined "*motor*" or "*somatosensory*" regions coded for stimulus identity, even as early as stimulus onset time. These results are consistent with our findings. If segregated region-function mapping was an accurate description of the brain, we would observe a disjoint or at most a minimally overlapping organization. Instead, we found a substantially overlapping organization, consistent with the emerging view that brain functions may be implemented in a shared, distributed set of regions that are not easily segregable [58, 81, 82, 87–89].

Conclusion

Our multi-modal dataset allowed us to characterize the functional organization of the mouse cortex. We found that large-scale brain networks mapped using fMRI-BOLD, the most commonly used imaging method in humans, are reproduced by Ca^{2+} imaging, a signal with high neuronal specificity. The present data, combined with previous multi-modal results, demonstrate that blood oxygen signals detected by fMRI may serve as a reliable surrogate for neuronal signals, especially when studying the large-scale functional organization of the brain in a slow temporal frequency band.

Additionally, our data revealed a substantially overlapping network organization for the mouse cortex. The present multi-modal data from mice paired with previous findings in human literature confirms that the mammalian brain

is a system with an overlapping architecture: given the option, the majority of brain regions participated in multiple networks. Therefore, enforcing a disjoint organization leads to the loss of valuable information about the varying affiliation strength of brain regions in networks. Future studies should take this concept into consideration.

Acknowledgements

We would like to thank all members of the Multiscale Imaging and Spontaneous Activity in Cortex (MISAC) collaboration at Yale University. We thank P. Brown for valuable input on the design and building of the telecentric lens holder. We thank J. Greenwood and the Neurotechnology Core at Yale University for modifying and building optics associated with the telecentric lens. We thank A. DeSimone, P. Brown and the Yale School of Medicine electronics and machine shop. This work was supported by funding from the NIH R01 MH111424 (R.T.C., M.C. and F.H.), U01 N2094358 (M.C. and R.T.C.), as well as 1RF1NS130069 and R21AG075778 (EMRL). H. Vafaii's contribution to this research was supported in part by NSF award DGE-1632976.

References

[1] Marcus E. Raichle et al. "A default mode of brain function." In: *Proceedings of the National Academy of Sciences of the United States of America* 98 2 (2001), pp. 676–82.

[2] Michael D Fox et al. "The human brain is intrinsically organized into dynamic, anticorrelated functional networks". In: *Proceedings of the National Academy of Sciences* 102.27 (2005), pp. 9673–9678.

[3] Jessica S Damoiseaux et al. "Consistent resting-state networks across healthy subjects". In: *Proceedings of the national academy of sciences* 103.37 (2006), pp. 13848–13853.

[4] B. T. Thomas Yeo et al. "The organization of the human cerebral cortex estimated by intrinsic functional connectivity." In: *Journal of neurophysiology* 106 3 (2011), pp. 1125–65.

[5] Jonathan D. Power et al. "Functional Network Organization of the Human Brain". In: *Neuron* 72 (2011), pp. 665–678.

[6] Stephen M Smith et al. "Resting-state fMRI in the human connectome project". In: *Neuroimage* 80 (2013), pp. 144–168.

[7] Joshua Faskowitz et al. "Edge-centric functional network representations of human cerebral cortex reveal overlapping system-level architecture". In: *Nature Neuroscience* 23 (2020), pp. 1644–1654.

[8] R Matthew Hutchison et al. "Functional networks in the anesthetized rat brain revealed by independent component analysis of resting-state FMRI". In: *Journal of neurophysiology* 103.6 (2010), pp. 3398–3406.

[9] Brian R White et al. "Imaging of functional connectivity in the mouse brain". In: *PloS one* 6.1 (2011), e16322.

[10] Elisabeth Jonckers et al. "Functional connectivity fMRI of the rodent brain: comparison of functional connectivity networks in rat and mouse". In: *PloS one* 6.4 (2011), e18876.

[11] Lino Becerra et al. "Robust reproducible resting state networks in the awake rodent brain". In: *PloS one* 6.10 (2011), e25701.

[12] Mohammadreza Nasiriavanaki et al. "High-resolution photoacoustic tomography of resting-state functional connectivity in the mouse brain". In: *Proceedings of the National Academy of Sciences* 111.1 (2014), pp. 21–26.

[13] Francesco Sforazzini et al. "Distributed BOLD and CBV-weighted resting-state networks in the mouse brain". In: *NeuroImage* 87 (2014), pp. 403–415.

[14] Valerio Zerbi et al. "Mapping the mouse brain with rs-fMRI: An optimized pipeline for functional network identification". In: *NeuroImage* 123 (2015), pp. 11–21.

[15] Adam Sierakowiak et al. “Default mode network, motor network, dorsal and ventral basal ganglia networks in the rat brain: comparison to human networks using resting state-fMRI”. In: *PloS one* 10.3 (2015), e0120345.

[16] Adam Liska et al. “Functional connectivity hubs of the mouse brain”. In: *NeuroImage* 115 (2015), pp. 281–291.

[17] Ludovico Coletta et al. “Network structure of the mouse brain connectome with voxel resolution.” In: *Science advances* 6 51 (2020).

[18] Joanes Grandjean et al. “Common functional networks in the mouse brain revealed by multi-centre resting-state fMRI analysis”. In: *NeuroImage* 205 (2020).

[19] Joanes Grandjean et al. “StandardRat: A multi-center consensus protocol to enhance functional connectivity specificity in the rat brain”. In: *bioRxiv* (2022).

[20] Marcus E Raichle. “The brain’s default mode network”. In: *Annual review of neuroscience* 38 (2015), pp. 433–447.

[21] Jennifer D. Whitesell et al. “Regional, Layer, and Cell-Type-Specific Connectivity of the Mouse Default Mode Network”. In: *Neuron* 109 (2021), 545–559.e8.

[22] Aaron T Winder et al. “Weak correlations between hemodynamic signals and ongoing neural activity during the resting state”. In: *Nature neuroscience* 20.12 (2017), pp. 1761–1769.

[23] Patrick J Drew et al. “Ultra-slow oscillations in fMRI and resting-state connectivity: neuronal and vascular contributions and technical confounds”. In: *Neuron* 107.5 (2020), pp. 782–804.

[24] Patrick J Drew. “Neurovascular coupling: motive unknown”. In: *Trends in Neurosciences* (2022).

[25] Nikos K Logothetis and Brian A Wandell. “Interpreting the BOLD signal”. In: *Annu. Rev. Physiol.* 66 (2004), pp. 735–769.

[26] Nikos K Logothetis. “What we can do and what we cannot do with fMRI”. In: *Nature* 453.7197 (2008), pp. 869–878.

[27] Randy L. Buckner, Fenna M. Krienen, and B. T. Thomas Yeo. “Opportunities and limitations of intrinsic functional connectivity MRI”. In: *Nature Neuroscience* 16 (2013), pp. 832–837.

[28] Dimitri M Kullmann. “Editorial”. In: *Brain* 143.4 (Apr. 2020), pp. 1045–1045. ISSN: 0006-8950. DOI: 10.1093/brain/awaa082.

[29] Evelyn M. R. Lake et al. “Simultaneous cortex-wide fluorescence Ca^{2+} imaging and whole-brain fMRI”. In: *Nature methods* 17 (2020), pp. 1262–1271.

[30] Patricia Pais-Roldán et al. “Contribution of animal models toward understanding resting state functional connectivity”. In: *NeuroImage* 245 (2021).

[31] Teppei Matsui, Tomonari Murakami, and Kenichi Ohki. “Transient neuronal coactivations embedded in globally propagating waves underlie resting-state functional connectivity”. In: *Proceedings of the National Academy of Sciences* 113 (2016), pp. 6556–6561.

[32] Ying Ma et al. “Resting-state hemodynamics are spatiotemporally coupled to synchronized and symmetric neural activity in excitatory neurons”. In: *Proceedings of the National Academy of Sciences* 113 (2016), E8463–E8471.

[33] Matthew C Murphy et al. “Macroscale variation in resting-state neuronal activity and connectivity assessed by simultaneous calcium imaging, hemodynamic imaging and electrophysiology”. In: *Neuroimage* 169 (2018), pp. 352–362.

[34] Yi He et al. “Ultra-slow single-vessel BOLD and CBV-based fMRI spatiotemporal dynamics and their correlation with neuronal intracellular calcium signals”. In: *Neuron* 97.4 (2018), pp. 925–939.

[35] Zilu Ma et al. “Gaining insight into the neural basis of resting-state fMRI signal”. In: *Neuroimage* 250 (2022), p. 118960.

[36] Patrick W Wright et al. “Functional connectivity structure of cortical calcium dynamics in anesthetized and awake mice”. In: *PloS one* 12.10 (2017), e0185759.

[37] Lindsey M Brier et al. “Separability of calcium slow waves and functional connectivity during wake, sleep, and anesthesia”. In: *Neurophotonics* 6.3 (2019), p. 035002.

[38] Matthieu P Vanni et al. “Mesoscale mapping of mouse cortex reveals frequency-dependent cycling between distinct macroscale functional modules”. In: *Journal of Neuroscience* 37.31 (2017), pp. 7513–7533.

[39] Anish Mitra et al. “Spontaneous infra-slow brain activity has unique spatiotemporal dynamics and laminar structure”. In: *Neuron* 98.2 (2018), pp. 297–305.

[40] Gergely Palla et al. “Uncovering the overlapping community structure of complex networks in nature and society”. In: *nature* 435.7043 (2005), pp. 814–818.

[41] Albert-László Barabási, Natali Gulbahce, and Joseph Loscalzo. “Network medicine: a network-based approach to human disease”. In: *Nature reviews genetics* 12.1 (2011), pp. 56–68.

[42] Michael W Cole et al. “Multi-task connectivity reveals flexible hubs for adaptive task control”. In: *Nature neuroscience* 16.9 (2013), pp. 1348–1355.

[43] Evelina Fedorenko, John Duncan, and Nancy Kanwisher. “Broad domain generality in focal regions of frontal and parietal cortex”. In: *Proceedings of the National Academy of Sciences* 110.41 (2013), pp. 16616–16621.

[44] BT Thomas Yeo et al. “Functional specialization and flexibility in human association cortex”. In: *Cerebral cortex* 25.10 (2015), pp. 3654–3672.

[45] Mahshid Najafi et al. “Overlapping communities reveal rich structure in large-scale brain networks during rest and task conditions”. In: *NeuroImage* 135 (2016), pp. 92–106.

[46] B. T. Thomas Yeo et al. “Estimates of segregation and overlap of functional connectivity networks in the human cerebral cortex”. In: *NeuroImage* 88 (2014), pp. 212–227.

[47] Prem Gopalan and David M. Blei. “Efficient discovery of overlapping communities in massive networks”. In: *Proceedings of the National Academy of Sciences* 110 (2013), pp. 14534–14539.

[48] Martijn P van den Heuvel and Olaf Sporns. “Network hubs in the human brain”. In: *Trends in cognitive sciences* 17.12 (2013), pp. 683–696.

[49] Olaf Sporns. “Structure and function of complex brain networks”. In: *Dialogues in clinical neuroscience* (2022).

[50] Maxwell A. Bertolero, B. T. Thomas Yeo, and Mark D’Esposito. “The diverse club”. In: *Nature Communications* 8 (2017).

[51] Jonathan D. Power et al. “Evidence for Hubs in Human Functional Brain Networks”. In: *Neuron* 79 (2013), pp. 798–813.

[52] Quanxin Wang et al. “The Allen Mouse Brain Common Coordinate Framework: A 3D Reference Atlas”. In: *Cell* 181 (2020), 936–953.e20.

[53] Gabriel Desrosiers-Gregoire et al. “Rodent Automated Bold Improvement of EPI Sequences (RABIES): A standardized image processing and data quality platform for rodent fMRI.” In: *bioRxiv* (2022).

[54] D O’Connor et al. “Functional network properties derived from wide-field calcium imaging differ with wakefulness and across cell type”. In: *NeuroImage* 264 (2022), p. 119735. ISSN: 1053-8119. DOI: 10.1016/j.neuroimage.2022.119735.

[55] Edo M Airoldi et al. “Mixed membership stochastic blockmodels”. In: *Advances in neural information processing systems* 21 (2008).

[56] Kazunori O’Hashi et al. “Construction of the common cortical space by spontaneous activity and its application in the mouse cortex”. In: *Biochemical and biophysical research communications* 513.4 (2019), pp. 869–874.

[57] Tsai-Wen Chen et al. “A Map of Anticipatory Activity in Mouse Motor Cortex”. In: *Neuron* 94 (2017), 866–879.e4.

[58] William E Allen et al. “Global representations of goal-directed behavior in distinct cell types of mouse neocortex”. In: *Neuron* 94.4 (2017), pp. 891–907.

[59] Hiroshi Makino et al. “Transformation of cortex-wide emergent properties during motor learning”. In: *Neuron* 94.4 (2017), pp. 880–890.
[60] Hidehiko K. Inagaki et al. “Neural Algorithms and Circuits for Motor Planning.” In: *Annual review of neuroscience* (2022).
[61] Michael Brecht. “Movement, Confusion, and Orienting in Frontal Cortices”. In: *Neuron* 72 (2011), pp. 193–196.
[62] Florent Barthas and A. Kwan. “Secondary Motor Cortex: Where ‘Sensory’ Meets ‘Motor’ in the Rodent Frontal Cortex”. In: *Trends in Neurosciences* 40 (2017), pp. 181–193.
[63] Takashi R Sato et al. “Interhemispherically dynamic representation of an eye movement-related activity in mouse frontal cortex”. In: *eLife* 8 (2019).
[64] Andrea Lancichinetti and Santo Fortunato. “Benchmarks for testing community detection algorithms on directed and weighted graphs with overlapping communities.” In: *Physical review. E, Statistical, nonlinear, and soft matter physics* 80 1 Pt 2 (2009), p. 016118.
[65] Eyal Bergmann et al. “Individual variability in functional connectivity architecture of the mouse brain”. In: *Communications Biology* 3 (2020).
[66] Sophia Mueller et al. “Individual Variability in Functional Connectivity Architecture of the Human Brain”. In: *Neuron* 77 (2013), pp. 586–595.
[67] Randy L. Buckner et al. “Cortical Hubs Revealed by Intrinsic Functional Connectivity: Mapping, Assessment of Stability, and Relation to Alzheimer’s Disease”. In: *The Journal of Neuroscience* 29 (2009), pp. 1860–1873.
[68] Jaewon Yang and Jure Leskovec. “Overlapping communities explain core–periphery organization of networks”. In: *Proceedings of the IEEE* 102.12 (2014), pp. 1892–1902.
[69] Alessandro Gozzi and Adam J. Schwarz. “Large-scale functional connectivity networks in the rodent brain”. In: *NeuroImage* 127 (2016), pp. 496–509.
[70] Julia V Cramer et al. “In vivo widefield calcium imaging of the mouse cortex for analysis of network connectivity in health and brain disease”. In: *Neuroimage* 199 (2019), pp. 570–584.
[71] Daniel Gutierrez-Barragan et al. “Infraslow State Fluctuations Govern Spontaneous fMRI Network Dynamics”. In: *Current Biology* 29 (2019), 2295–2306.e5.
[72] Jessica R Andrews-Hanna et al. “Functional-anatomic fractionation of the brain’s default network”. In: *Neuron* 65.4 (2010), pp. 550–562.
[73] Rodrigo M Braga and Randy L Buckner. “Parallel interdigitated distributed networks within the individual estimated by intrinsic functional connectivity”. In: *Neuron* 95.2 (2017), pp. 457–471.
[74] Dmitry R. Lyamzin and Andrea Benucci. “The mouse posterior parietal cortex: anatomy and functions”. In: *Neuroscience research* 140 (2018), pp. 14–22.
[75] Christopher Blöcker, Juan Carlos Nieves, and Martin Rosvall. “Map equation centrality: community-aware centrality based on the map equation”. In: *Applied Network Science* 7.1 (2022), pp. 1–24.
[76] Roger Guimerà and Luis A. Nunes Amaral. “Functional cartography of complex metabolic networks”. In: *Nature* 433 (2005), pp. 895–900.
[77] Daniel Gutierrez-Barragan et al. “Unique spatiotemporal fMRI dynamics in the awake mouse brain”. In: *Current Biology* 32 (2022), 631–644.e6.
[78] Jonathan D Power et al. “Methods to detect, characterize, and remove motion artifact in resting state fMRI”. In: *Neuroimage* 84 (2014), pp. 320–341.
[79] Paul Broca et al. “Perte de la parole, ramollissement chronique et destruction partielle du lobe antérieur gauche du cerveau”. In: *Bull Soc Anthropol* 2.1 (1861), pp. 235–238.
[80] Korbinian Brodmann. *Vergleichende Lokalisationslehre der Grosshirnrinde in ihren Prinzipien dargestellt auf Grund des Zellenbaues*. Barth, 1909.
[81] Luiz Pessoa. “Understanding brain networks and brain organization.” In: *Physics of life reviews* 11 3 (2014), pp. 400–35.

[82] Michael L Anderson. "Précis of after phrenology: neural reuse and the interactive brain". In: *Behavioral and Brain Sciences* 39 (2016).
[83] Edward Zagha et al. "The Importance of Accounting for Movement When Relating Neuronal Activity to Sensory and Cognitive Processes". In: *The Journal of Neuroscience* 42 (2022), pp. 1375–1382.
[84] Carsen Stringer et al. "Spontaneous behaviors drive multidimensional, brainwide activity". In: *Science* 364 (2019).
[85] Philip R. L. Parker et al. "Movement-Related Signals in Sensory Areas: Roles in Natural Behavior". In: *Trends in Neurosciences* 43 (2020), pp. 581–595.
[86] Sadegh Ebrahimi et al. "Emergent reliability in sensory cortical coding and inter-area communication". In: *Nature* 605.7911 (2022), pp. 713–721.
[87] Terrence J Sejnowski, Christof Koch, and Patricia S Churchland. "Computational neuroscience". In: *Science* 241.4871 (1988), pp. 1299–1306.
[88] M-Marsel Mesulam. "Large-scale neurocognitive networks and distributed processing for attention, language, and memory". In: *Annals of Neurology: Official Journal of the American Neurological Association and the Child Neurology Society* 28.5 (1990), pp. 597–613.
[89] Paul Cisek and John F. Kalaska. "Neural mechanisms for interacting with a world full of action choices." In: *Annual review of neuroscience* 33 (2010), pp. 269–98.
[90] Brian B Avants, Nick Tustison, Gang Song, et al. "Advanced normalization tools (ANTS)". In: *Insight j* 2.365 (2009), pp. 1–35.
[91] Joseph E. Knox et al. "High-resolution data-driven model of the mouse connectome". In: *Network Neuroscience* 3 (2018), pp. 217–236.
[92] Ofer Yizhar et al. "Optogenetics in Neural Systems". In: *Neuron* 71 (2011), pp. 9–34.
[93] Chi Ren and Takaki Komiyama. "Characterizing Cortex-Wide Dynamics with Wide-Field Calcium Imaging". In: *The Journal of Neuroscience* 41 (2021), pp. 4160–4168.
[94] Daniel Barson et al. "Simultaneous mesoscopic and two-photon imaging of neuronal activity in cortical circuits". In: *Nature methods* 17 (2019), pp. 107–113.
[95] Andrew J. Peters et al. "Striatal activity topographically reflects cortical activity." In: *Nature* (2021).
[96] Martijn P. van den Heuvel et al. "Proportional thresholding in resting-state fMRI functional connectivity networks and consequences for patient-control connectome studies: Issues and recommendations". In: *NeuroImage* 152 (2017), pp. 437–449.
[97] Prem Gopalan et al. "Scalable Inference of Overlapping Communities". In: *NIPS*. 2012.
[98] Matthew D Hoffman et al. "Stochastic variational inference". In: *Journal of Machine Learning Research* (2013).
[99] David M. Blei, Alp Kucukelbir, and Jon D. McAuliffe. "Variational Inference: A Review for Statisticians". In: *Journal of the American Statistical Association* 112 (2016), pp. 859–877.
[100] Varun Saravanan, Gordon J. Berman, and Samuel J. Sober. "Application of the Hierarchical Bootstrap to Multi-Level Data in Neuroscience". In: *bioRxiv* (2020).
[101] Bradley Efron. "Nonparametric standard errors and confidence intervals". In: *canadian Journal of Statistics* 9.2 (1981), pp. 139–158.
[102] Bradley Efron. *The jackknife, the bootstrap and other resampling plans*. SIAM, 1982.
[103] Bradley Efron. "Better bootstrap confidence intervals". In: *Journal of the American statistical Association* 82.397 (1987), pp. 171–185.
[104] Yoav Benjamini and Yosef Hochberg. "Controlling the false discovery rate: a practical and powerful approach to multiple testing". In: *Journal of the royal statistical society series b-methodological* 57 (1995), pp. 289–300.
[105] Sture Holm. "A simple sequentially rejective multiple test procedure". In: *Scandinavian journal of statistics* (1979), pp. 65–70.

[106] Ulrike Von Luxburg, Robert C Williamson, and Isabelle Guyon. "Clustering: Science or art?" In: *Proceedings of ICML workshop on unsupervised and transfer learning*. JMLR Workshop and Conference Proceedings. 2012, pp. 65–79.
[107] Xiaoran Yan et al. "Weight thresholding on complex networks". In: *Phys. Rev. E* 98 (4 Oct. 2018), p. 042304. DOI: 10.1103/PhysRevE.98.042304.
[108] Kristoffer J Albers et al. "Using connectomics for predictive assessment of brain parcellations". In: *NeuroImage* 238 (2021), p. 118170.
[109] Julie A Harris et al. "Hierarchical organization of cortical and thalamic connectivity". In: *Nature* 575.7781 (2019), pp. 195–202.
[110] Evan M. Gordon et al. "Precision Functional Mapping of Individual Human Brains". In: *Neuron* 95 (2017), 791–807.e7.
[111] Marija Markicevic et al. "Emerging imaging methods to study whole-brain function in rodent models". In: *Translational Psychiatry* 11 (2021).

Materials and methods

Animals

Mice were group housed on a 12-hour light/dark cycle. Food and water were available *ad libitum*. Cages were individually ventilated. Animals were 6-8 weeks old, 25-30g, at the time of the first imaging session. Animals (SLC, Slc17a7-cre/Camk2α-tTA/TITL-GCaMP6f also known as Slc17a7-cre/Camk2α-tTA/Ai93) were generated from parent 1 (Slc17a7-IRES2-Cre-D) and parent 2 (Ai93(TITL-GCaMP6f)-D;CaMK2a-tTA). Both were on a C57BL/6J background. To generate these animals, male CRE mice were selected from the offspring of parents with different genotypes, which is necessary to avoid leaking of CRE expression. Animals were purchased from Jackson Labs

Head-plate surgery

All mice underwent a minimally invasive surgical procedure enabling permanent optical access to the cortical surface (previously described here: [29]). Briefly, mice were anesthetized with 5% isoflurane (70/30 medical air/O2) and head-fixed in a stereotaxic frame (KOPF). After immobilization, isoflurane was reduced to 2%. Paralube was applied to the eyes to prevent dryness, meloxicam (2 mg/kg body weight) was administered subcutaneously, and bupivacaine (0.1%) was injected under the scalp (incision site). Hair was removed (NairTM) from the surgical site and the scalp washed with betadine followed by ethanol 70% (three times). The scalp was removed along with the soft tissue overlying the skull and the upper portion of the neck muscle. Exposed skull tissue was cleaned and dried. Antibiotic powder (Neo-Predef) was applied to the incision site, and isoflurane was further reduced to 1.5%. Skull-thinning of the frontal and parietal skull plates was performed using a hand-held drill (FST, tip diameter: 1.4 and 0.7 mm). Superglue (Locite) was applied to the exposed skull, followed by transparent dental cement (C&B Metabond®, Parkell) once the glue dried. A custom in-house built head-plate was affixed using dental cement. The head-plate was composed of a double-dovetail plastic frame (acrylonitrile butadiene styrene plastic, TAZ-5 printer, 0.35 mm nozzle, Lulzbot) and a hand-cut microscope slide designed to match the size and shape of the mouse skull. Mice were allotted at least 7 days to recover from head-plate implant surgery before undergoing the first of three multi-modal imaging sessions.

Multi-modal image acquisition

All mice, $N = 10$, underwent three multi-modal imaging sessions with a minimum of 7 days between acquisitions. During each acquisition, we simultaneously acquired fMRI BOLD and wide-field Ca^{2+} imaging data using a

custom apparatus and imaging protocol we have described previously [29]. Functional MRI data were acquired on an 11.7T system (Bruker, Billerica, MA), using ParaVision version 6.0.1 software. During each imaging session, 4 functional runs (10 min each) were acquired. Structural MRI data were acquired to allow both multi-modal registration and registration to a common space. Mice were scanned while lightly anesthetized ($0.5 - 1.25\%$ isoflurane in 30/70 O2/medical air) and freely breathing. Body temperature was monitored (Neoptix fiber) and maintained with a circulating water bath.

Functional MRI

We employed a gradient-echo, echo-planar-imaging sequence with a 1.0 sec repetition time (TR) and 9.1 ms echo time (TE). Isotropic data (0.4 mm x 0.4 mm x 0.4 mm) were acquired along 28 slices providing near whole-brain coverage.

Structural MRI

We acquired 4 structural images for multi-modal data registration and registration to a common space. (1) A multi-spin-multi-echo (MSME) image sharing the same FOV as the fMRI data, with a TR/TE of 2500/20ms, 28 slices, two averages, and resolution of 0.1 mm x 0.1 mm x 0.4 mm. (2) A whole-brain isotropic (0.2 mm x 0.2 mm x 0.2 mm) 3D MSME image with a TR/TE of 5500/20ms, 78 slices, and 2 averages. (3) A fast-low-angle-shot (FLASH) time-of-flight (TOF) angiogram with a TR/TE of 130/4ms, resolution of 0.05 mm × 0.05 mm × 0.05 mm and FOV of 2.0 cm × 1.0 cm × 2.5 cm (positioned to capture the cortical surface). (4) A FLASH image of the angiogram FOV, including four averages, with a TR/TE of 61/7ms, and resolution of 0.1 mm × 0.1 mm × 0.1 mm.

Wide-field fluorescence Ca^{2+} imaging

Data were recorded using CamWare version 3.17 at an effective rate of 10 Hz. To enable frame-by-frame background correction, violet (395/25, Ca^{2+}-insensitive) and cyan (470/24, Ca^{2+}-sensitive) illumination (controlled by an LLE 7Ch Controller from Lumencor) were interleaved at a rate of 20 Hz. The exposure time for each channel (violet and cyan) was 40 ms to avoid artifacts caused by the rolling shutter refreshing. Thus, the sequence was: 10 ms blank, 40 ms violet, 10 ms blank, 40 ms cyan, and so on. The custom-built optical components used for in-scanner wide-field Ca^{2+} imaging have been described previously [29].

Image preprocessing

multi-modal data registration

All steps are executed using tools in BioImage Suite (BIS) specifically designed for this purpose [29]. For each animal, and each imaging session, the MR angiogram is masked and used to generate a view that recapitulates what the cortical surface would look like in 2D from above. This treatment of the data highlights the vascular architecture on the surface of the brain (notably the projections of the middle cerebral arteries, MCA) which are also visible in the static wide-field Ca^{2+} imaging data. Using these and other anatomical landmarks, we generate a linear transform that aligns the MR and wide-field Ca^{2+} imaging data. The same static wide-field image is used as a reference for correcting motion in the time series. To register the anatomical and functional MRI data, linear transforms are generated and then concatenated before being applied. Data are registered to a common space (CCFv3) using the isotropic whole-brain MSME image and a non-linear registration.

Fluorescence Ca^{2+} imaging data preprocessing

We have previously described all steps in this pipeline [54]. Briefly, the raw signal is split between GCaMP-sensitive and GCaMP-insensitive imaging frames. Spatial smoothing with a large kernel (16-pixel kernel, median filter) is applied to reduce and/or remove focal artifacts (e.g., dust or dead pixels from broken fibers). These do not move with the subject and can bias motion correction. Motion correction parameters are estimated on these data using normalized mutual information. Rigid image registration is performed between each imaging frame in the time series and the reference frame. Registration parameters are saved, and the large kernel-smoothed images are discarded. Modest spatial smoothing (4-pixel kernel, median filter) is applied to the raw data, and these data are motion corrected by applying the parameters estimated in the previous step. Data are down-sampled by a factor of two in both spatial dimensions. Photo bleach correction is applied to reduce the exponential decay in fluorescence at the onset of imaging. The fluorophore-insensitive time series is regressed from the fluorophore-sensitive time series. 50 seconds are discarded from the beginning of the time series to avoid filtering-related edge artifacts. Data are scrubbed for motion based on estimates from the fMRI time series where a conservative 0.2mm threshold is applied. Runs are removed from the data pool if $1/2$ imaging frames exceed this threshold. In this dataset, 5 runs (or $\sim 4\%$ of all runs) were removed for this reason.

RABIES fMRI data preprocessing

For fMRI preprocessing, we used RABIES (Rodent automated BOLD improvement of EPI sequences) v0.4.2 [53]. We applied structural and functional inhomogeneity correction N3 (nonparametric nonuniform intensity normalization), motion correction (ANTS, Advanced normalization tools) [90], and slice time correction, all in native space. A common space was created by nonlinearly registering and averaging the isotropic MSME anatomical images (one from each mouse/session), which was registered to the Allen CCfv3 common space using a nonlinear transformation.

For each run, fMRI data are motion corrected and averaged to create a representative mean image. Each frame in the time series is registered to this reference. To move the fMRI data to the common space, the representative mean image is registered to the isotropic structural MSME image acquired during the same imaging session. This procedure minimizes the effects of distortions caused by susceptibility artifacts. Then, the three transforms - (1) representative mean to individual mouse/session isotropic MSME image, (2) individual mouse/session isotropic MSME image to within-dataset common space, and (3) within-dataset common space to out-of-sample common space – are concatenated and applied to the fMRI data. Functional data (0.4mm isotropic) were upsampled to match anatomical MR image resolution (0.2mm isotropic). Registration performance was visually inspected and verified for all sessions. Motion is regressed (6 parameters). Data are high-pass filtered (3rd order Butterworth) between [0.01-0.5] Hz, and 30 seconds are discarded from both the beginning and end of the time series to avoid filtering-related edge artifacts and white matter + ventricles regression is applied. Data are scrubbed for motion using a conservative 0.1mm threshold. Runs are removed from the data pool if half imaging frames exceed this threshold for a given run. In this dataset, 5 runs (or $\sim 4\%$ of all runs) are removed for this reason.

Parcellating the cortex into columnar regions of interest (ROI)

To create regions of interest (ROIs), we employed the Allen CCFv3 (2017) space given its use by the research community [52]. (1) We generated a cortical flatmap within the CCFv3 space [52] following the procedure outlined by [91] (`https://github.com/AllenInstitute/mouse_connectivity_models`). (2) We subdivided the left hemisphere into N regions via k-means clustering applied to pixel coordinates (for most analyses reported, $N = 512$). The right hemisphere was obtained by simple mirror-reversal to obtain a total of $2N$ regions. (3) Depth was added to the ROIs to obtain column-shaped regions. To do so, a path was generated by following streamlines normal to the surface descending in the direction of white matter (streamline paths were available at 10 μm res-

olution in CCFv3; see Figure 3F in [52]). Here, we chose ROI depth so that we included potential signals from layers 1 to 4 (layer masks were obtained from CCFv3). Evidence from wide-field Ca^{2+} imaging suggests that signals originate from superficial layers but can extend into the cortex to some extent [92–95]. (4) ROIs were downsampled from 10 μm to 100 μm resolution, which was used for co-registration of the individual brains (see SI for more details). After co-registration, ROIs were brought into the 3D fMRI individual spaces using an affine step followed by a nonlinear transformation. Then, for each individual, the ROIs were transformed from their 3D MR space into the 2D optical space (see above).

Functional network construction

Time series data were extracted and averaged from all voxels/pixels within an ROI in native space to generate a representative time series per ROI. For each modality, for each run, an adjacency matrix was calculated by applying Pearson correlation to time series data to each ROI pair. Next, we binarized the adjacency matrices by rank ordering the connection weights and maintaining the top 15%; thus, after binarization, the resulting graphs had a fixed density of $d = 15\%$ across all runs and modalities. This approach aims to keep the density of links fixed across individuals and runs and better preserves network properties compared to absolute thresholding [96]. To establish the robustness of our results to threshold values, we also tested values of 10% to 25% in 5% increments.

Finding overlapping communities

Overlapping network analysis was applied by using SVINET, a mixed-membership stochastic blockmodel algorithm [47, 97], which we previously applied to human fMRI data [45]. SVINET models the observed graph within a latent variable framework by assuming that the existence (or non-existence) of links between pairs of nodes can be explained by their latent community memberships. For binary adjacency matrix A and membership matrix π, the model assumes the conditional probability of a connection as follows

$$p(A_{ij}|\pi_i, \pi_j) \propto \sum_{k=1}^{K} \pi_{ik}\pi_{jk}, \tag{1}$$

where K is the number of communities, and $A_{ij} = 1$ if nodes i and j are connected and 0 otherwise. Intuitively, pairs of nodes are more likely to be connected if they belong to the same network or to (possibly several) overlapping networks. For example, in Figure 1E, nodes A and B have a link between them most likely because they both have nonzero membership strength in the green community. Nodes B and C are even more likely to have a link because they share membership in two communities together (red and blue). More formally, SVINET assumes the following generative process

1. For each node, draw community memberships $\pi_i \sim \text{Dirichlet}(\alpha)$
2. For each pair of nodes i and j:
   (a) Draw community indicator $z_{i\to j} \sim \pi_i$
   (b) Draw community indicator $z_{i\leftarrow j} \sim \pi_j$
   (c) Assign link between i and j if $z_{i\to j} = z_{i\leftarrow j}$.

Stochastic gradient ascent is used to fit model parameters α [98, 99]. Because model fitting is stochastic, we applied the algorithm to data from each run using 500 different random seeds.

Aligning community results

When applying community detection, a classic problem in computer science is that of matching the networks found upon multiple applications to related data (say, from different animals). Even if the networks found were identical, they could be generated in a different order, such that network 1 from one animal would be identical to network 7 from a second animal, say. Therefore, an algorithm is needed to find that network 7 corresponds most closely to network 1, and so on. Here, due to the stochastic nature of the algorithm, the resulting communities will be slightly different and possibly permuted versions of one another for each random seed of the algorithm.

Our algorithm worked as follows. For each run and random seed, membership vectors for all random seeds were submitted to k-means clustering (sklearn.cluster.KMeans) to determine K clusters (e.g., $K = 7$ for analyses with 7 networks). The similarity between the resulting cluster centroids was then established via cosine similarity, and the networks matched based on maximum similarity. Formally, the outcome membership matrix π per run.

Group results

Crucially, all these measures are computed at the run level first before combining at the group level.

Membership matrices

This is what's visualized in Figure 2A and C, Figure S1 and Figure S3A and C.

Thresholding membership values

Membership values were thresholded based on statistical significance. This step was adopted to enhance the robustness of our estimates of network overlap. For example, although a region with membership values $(0.05, 0.05, 0.05, 0.0$ could be considered as exhibiting membership to all networks, the values of the first four could be rather unreliable. Thus, membership values were thresholded to zero if they did not pass a test rejecting the null hypothesis that the value was zero. After thresholding, the surviving membership values were rescaled so as to sum to 1. Thresholding was performed for each animal separately by performing a one-sample t-test and employing a false discovery rate of 5%. All results shown utilized this step, with the exception of figures which illustrate the spatial patterns of membership values (and does not estimate network overlap). Not that almost all (around 99%) membership values that did not reach significance had values in the range (0, 0.2].

Region functional diversity

Similar to above, we apply Shannon entropy to membership matrix for each run separately before averaging. That is, given a membership matrix π from a run, we compute node entropies to get an entropy estimate per node at the run level

$$\text{(normalized) entropy of node } i \text{ at run level} = f(\pi_i) \equiv h_i = -\sum_{k=1}^{K} \pi_{ik} \log \pi_{ik} / \log K \tag{2}$$

We then average entropy estimates from all runs to get the group-level estimates. This is what's visualized in Figure 5B, and these group-level values are also used to calculate the correlations between modalities Figure 5C.

To visualize the entropy distribution, we take each h_i from a run and compute percentage values using 50 bins of width 0.02 that cover the entire range of valid entropy values $[0, 1]$. Once we calculate histogram values per run, we then average over the runs to get group-level estimates shown in Figure 5A. This is done in an identical way to other distributions reported in this work.

Statistical analysis

Hierarchical bootstrapping

Statistical results were performed at the group level by taking into consideration the hierarchical structure of the data (for each animal, runs within sessions), which can be naturally incorporated into computational bootstrapping to estimate variability respecting the organization of the data [100]. For each iteration (total of $1,000,000$), we sampled (with replacement) $N = 10$ animals, $N = 3$ sessions, and $N = 4$ runs, while guaranteeing sessions were yoked to the animal selected and runs were yoked to the session selected (Figure 1B). In this manner, the multiple runs were always from the same session, which originated from a specific animal. Overall, the procedure allowed us to estimate population-level variability based on the particular sample studied here. To estimate 95% confidence intervals, we used the bias-corrected and accelerated (BCa) method [101–103], which is particularly effective when relatively small sample sizes are considered (SciPy's scipy.stats.bootstrap). See figures Figure 2D-F, Figure 3B, Figure 5C, Figure 6C, Figure 7, Figure S3D-F, Figure S4, and Figure S6.

One-sample t-test

We used a one-sample t-test to define belonging in communities as a function of a threshold μ. The t-statistic for membership of node i in community k is given as

$$t_{ik} = \frac{\bar{\pi}_{ik} - \mu}{SE_{ik}}, \tag{3}$$

where $\bar{\pi}_{ik}$ is the group averaged membership of node i in community k, and SE_{ik} is the standard error estimated using hierarchical bootstrapping (see above). We calculated p values using t-statistics for all nodes and communities and declared a node a member of a community if its p-value reached significance $p = 0.05$. The results as a function of various μ are shown in Figure 4A. We applied Benjamini-Hochberg correction [104] using Python statsmodels' implementation (statsmodels.stats.multitest.multipletests) to correct for multiple comparison.

LFR analysis

The following parameters need to be specified to generate a binary and overlapping LFR graph. N, number of nodes; k, average degree; μ topological mixing parameter; t_1, minus exponent for the degree sequence; t_2 minus exponent for the community size distribution; C_{min}, minimum for the community sizes; C_{max}, maximum for the community sizes; ON, number of overlapping nodes; OM, number of memberships of the overlapping nodes.

To match basic statistics of the real data with LFR graphs we set $N = 542$; and, for every run from each data modality, we calculated the average degree k and estimated t_1 via an exponential fit to the degree distributions (scipy.stats). We set $t_2 = 0.1$, $C_{min} = 0.05 \times N \approx 27$, $C_{max} = 0.35 \times N \approx 190$. For the fraction of overlapping nodes, we explored a wide range between 0 (disjoint) and 0.9 in incremental steps of 0.1. This yielded $ON = 0$ up to $ON = 0.9 \times N = 488$. Finally, we used $OM = 2$ and 3. This results in a total of 20 LFR graphs per run, per data modality. We applied the community detection algorithm to LFR graphs in an identical way to the real data, but with fewer seeds ($N = 10$ compared to $N = 500$). The alignment procedure was performed in the same way as described above. See Figure S5.

Permutation test

We use a paired permutation test to compare conditions in Figure 2E and F, Figure S3E and F, and Figure S4; and to perform a node-wise comparison across modalities in Figure 5D. We used SciPy's implementation (scipy.stats.permutation_test) with $N = 1e6$ resamples. Holm–Bonferroni correction was applied to correct for multiple comparison [105].

Supplemental information

Supplementary discussion

Choosing number of networks

Clustering is in the eyes of the beholder (or the algorithm) [106]. Community detection is inherently ill-defined: algorithms do not find communities, what they do is "define" communities and later find them according to their definition. There is no "true" number of networks, as this largely depends on what you want to "do" later with them. Therefore, instead of focusing on a single result as a "true" decomposition, we explored network organization at different levels of granularity. We decided the number of communities empirically, using criteria such as bilateral symmetry. At the most coarse level, our $K = 3$ communities recapitulated previous seed-based reports in Ca^{2+} data, as well as coarse ICA reports in BOLD data. For $K = 7$ communities, our findings were similar to previous BOLD-ICA reports. The highly bilateral nature of our communities (even observed for up to $K = 20$ communities for Ca^{2+}) and their similarity to previous reports confirm that what we observed is real.

Thresholding the graphs

The algorithm used in this study requires binary graphs as its input [47], which necessitates choosing an edge-filtering threshold. To mitigate this, we employed an approach known as proportional thresholding which preserves the topology of the graphs better than alternatives such as absolute thresholding [96]. In addition, theoretical work has shown that network topology is highly robust against different thresholds [107]. Here we reported results at a graph density of $d = 15\%$. To ensure robustness of our findings to this arbitrary choice, we also explored densities going from $d = 10\%$ all the way up to $d = 25\%$ with incremental steps of 5%. Empirically, we found that our results were robust to the choice of edge density, as well as other hyperparameters. Thus, our data confirmed previous theoretical and simulation work that network topology is robust across a wide range of sparsity levels.

ROI definition scheme

Initially, we used brain regions defined in Allen Reference Atlas (ARA) as our ROIs [52]. However, we observed a considerable mismatch between functional parcellation and ARA parcellation. This is expected because ARA regions were delineated using various anatomical and structural criteria; but crucially, function was not one of them. Later, we switched to the spatially homogeneous parcellation scheme illustrated in Figure 1C and D. This significantly increased the robustness of our results, indicating that spatially homogeneous ROIs are more suitable for functional network construction. Our finding is consistent with previous reports in humans [108].

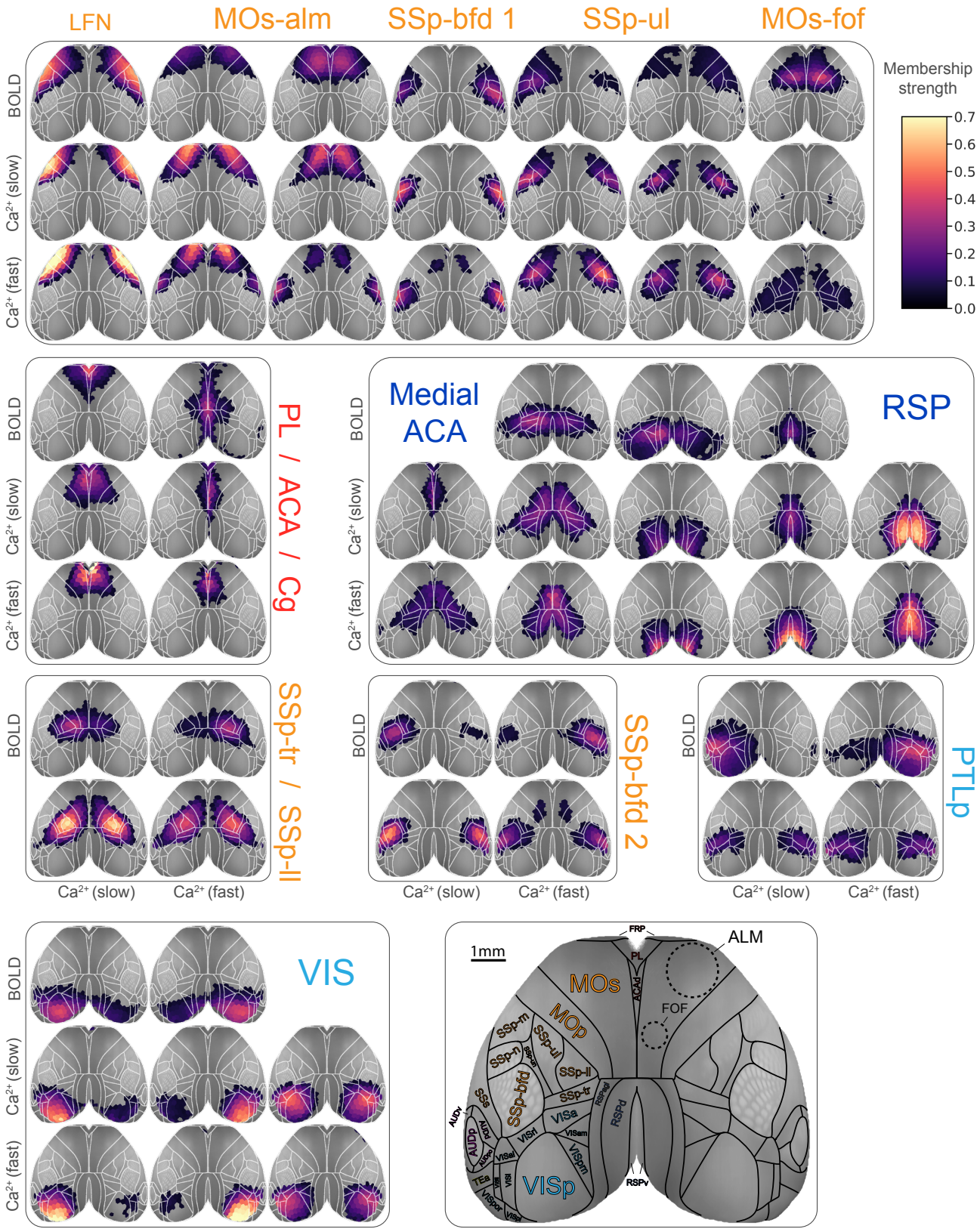

Figure S1: $K = 20$ networks solution. Even at $K = 20$, most networks still maintain a bilateral symmetry indicating the robustness of our results. This is especially true for Ca^{2+} data. A network centered around FOF appears as its own separate network for BOLD similar to $K = 7$ solution. However, we still don't see this network for Ca^{2+} . Instead, this region appears as part of large medial networks that span parts of SSp-tr/ll. Label colors inspired from Figure 1F in ref. [109]. Compare with Figure 2.

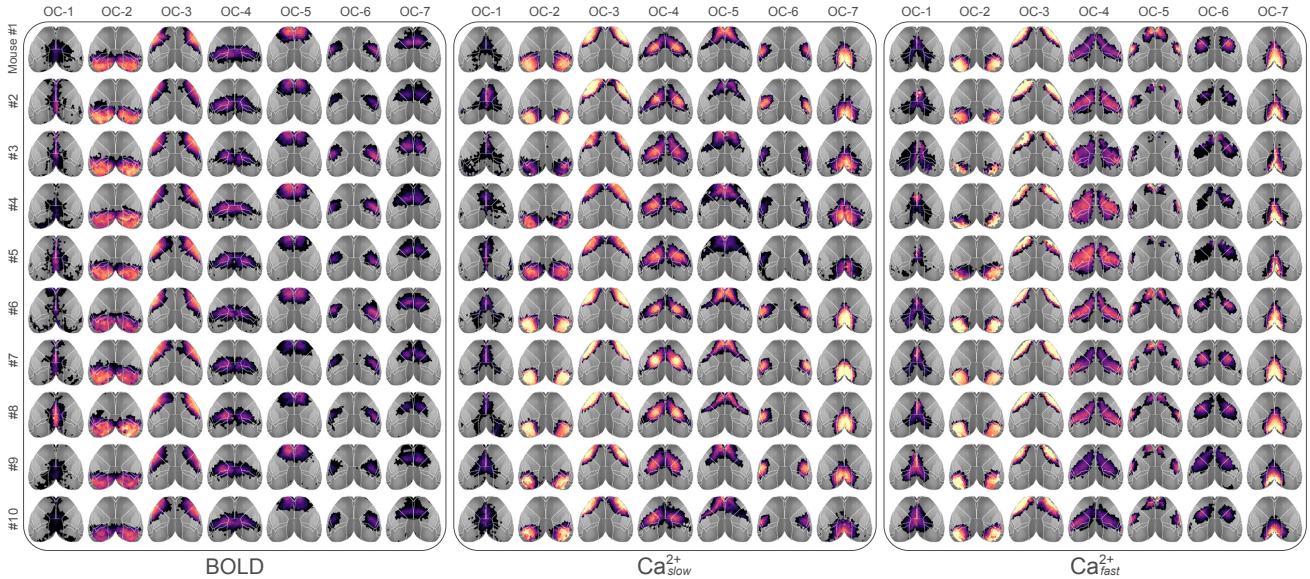

Figure S 2: Overlapping networks at the level of individuals. Each mouse was highly sampled (see Figure 1B), which allowed robust estimation of individualized networks. The high similarity of network structures across individuals is anticipated, as these mice are genetically very similar. However, there are still visible differences that would enable identification of individual mice from their network structure. Precision imaging has emerged as an important venue of investigation in humans [110]. Given the translational potential of mice [30, 111], we will investigate this direction more thoroughly in future work. See Figure 2C for group results.

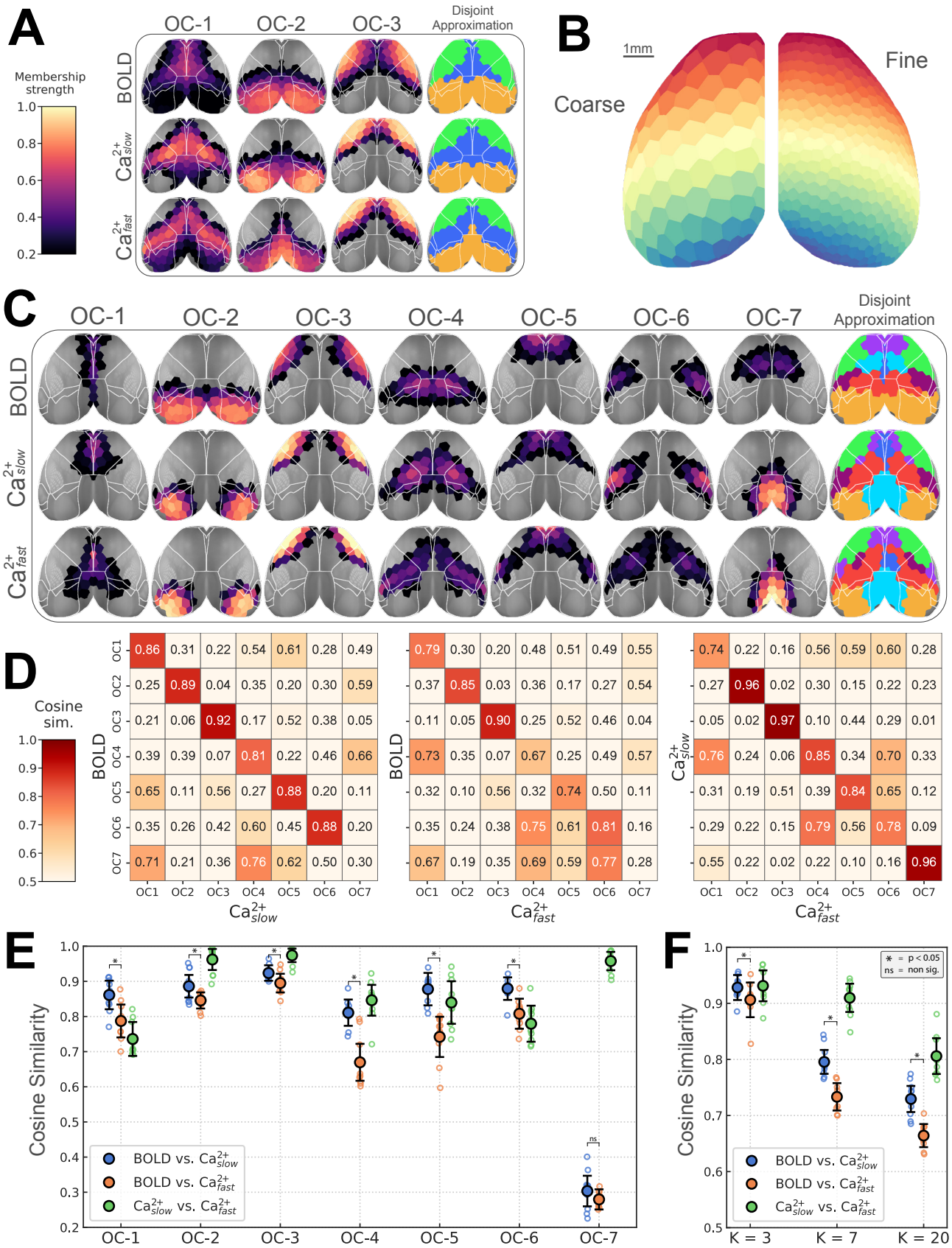

Figure S3: Network structure is robust to the choice of ROI granularity. **(A, C-F)** Similar to Figure 2. **(B)** Left, results with coarse ROIs are presented here; Right, fine ROIs were used for the main results. See also Figure S4.

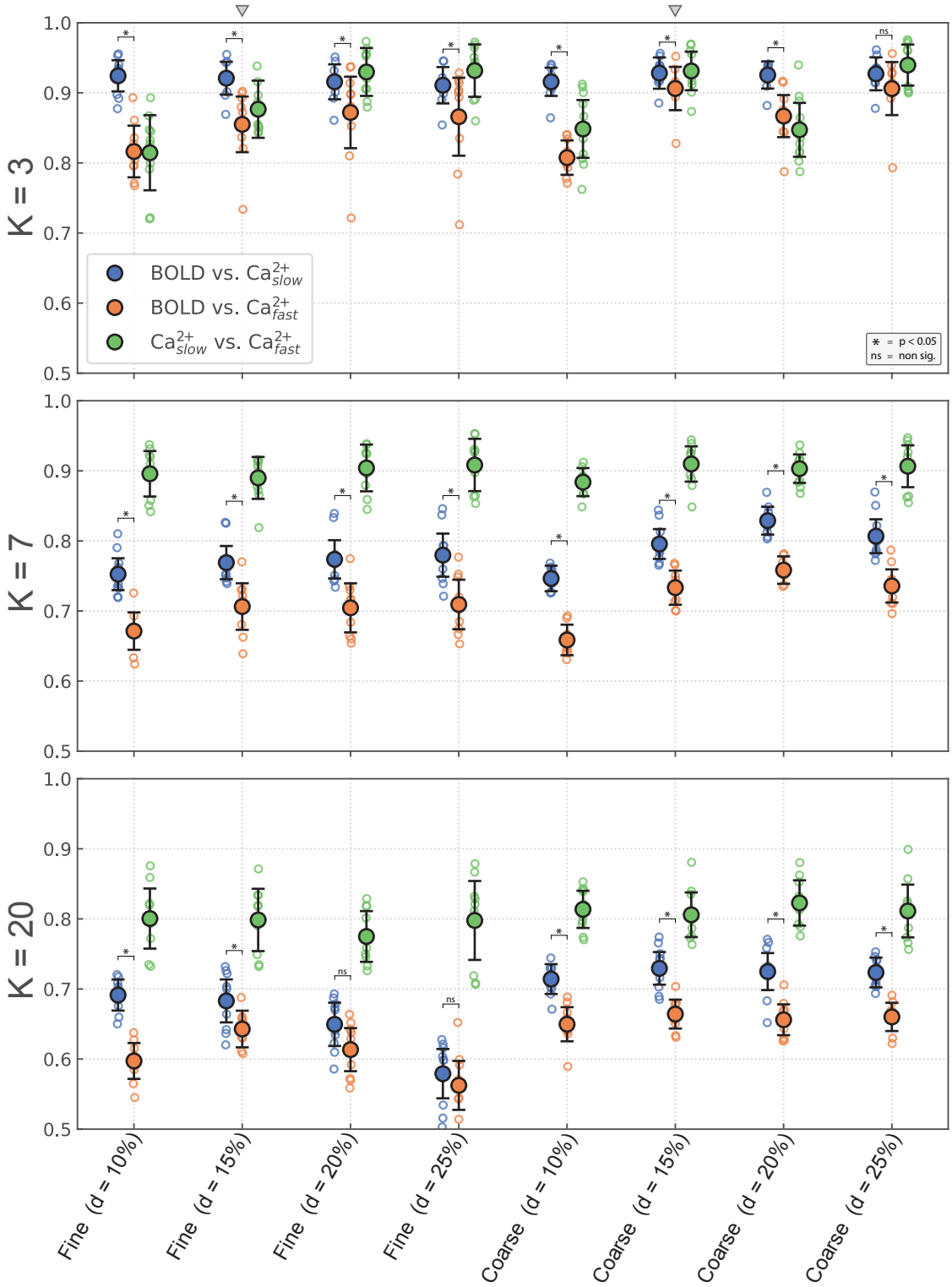

Figure S4: BOLD network organization is more similar to Ca^{2+}_{slow} than it is to Ca^{2+}_{fast} . This is a robust prediction of our study as it is reproduced over a large combinatorial space of analysis conditions. The y-axis is cosine similarity and the x-axis corresponds to different conditions. See Figure S3B for a visual comparison of coarse versus fine ROIs. d is graph density after the binarization step. Small triangles indicate our choice for the main results: $d = 15\%$, fine ROIs. Permutation test, $p < 0.05$, Holm-Bonferroni corrected. Error bars show 95% confidence intervals, hierarchical bootstrap. See also Figure 2 and Figure S3.

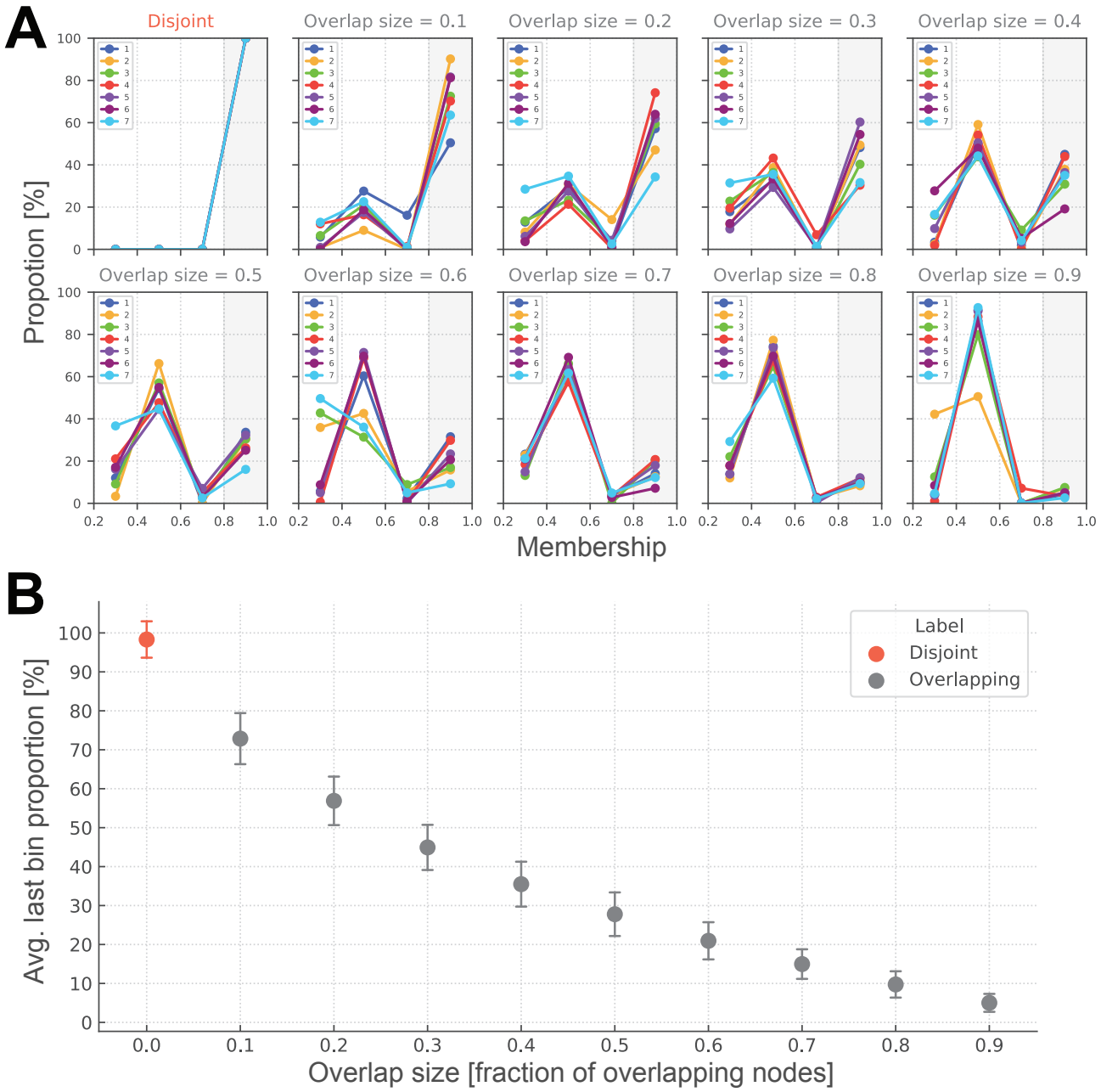

Figure S5: Verifying our analysis procedure using synthetic LFR graphs [64]. **(A)** To compute the distribution of node memberships, we divided the range $[0.2, 1.0]$ into four equal-sized bins. This binning scheme was chosen such that for disjoint graphs, the proportions are 100% in the last bin and 0% in all other bins. Overlap size, or fraction of overlapping nodes, is a tunable parameter in LFR graphs. Here we show how the distributions change as a function of overlap size. **(B)** We averaged the last bin proportions across all communities to get a single statistic per graph. Its mean over thousands of simulated graphs is shown here. The average last bin proportion drops as overlap size increases, thus making it a reliable proxy for network overlap size. Error bars indicate standard deviation. Compare with Figure 3.

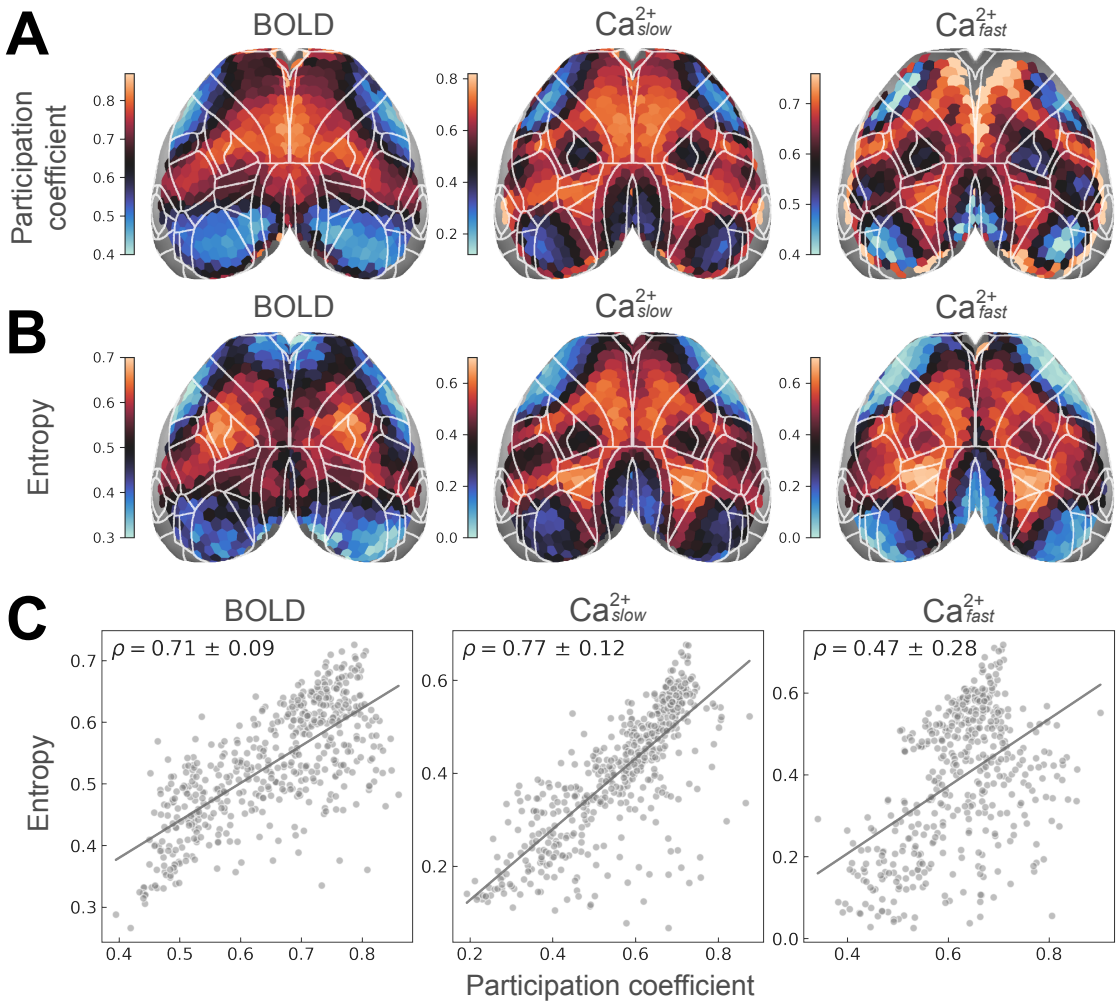

Figure S 6: Participation coefficient and entropy maps have similar organization. **(A)** Participation coefficient is a measure that quantifies link diversity when disjoint community detection algorithms are used [51, 76]. Note that for low-degree nodes with degree < 7, participation coefficient estimates become unreliable. For example, see frontal regions of Ca^{2+}_{fast} . **(B)** Entropy maps are from Figure 5, also shown here to visually aid comparison with part A. **(C)** Large correlation between the two centrality measures demonstrates that they capture the same underlying phenomenon and thus can be used interchangeably. This is especially visible for BOLD and Ca^{2+}_{slow} .

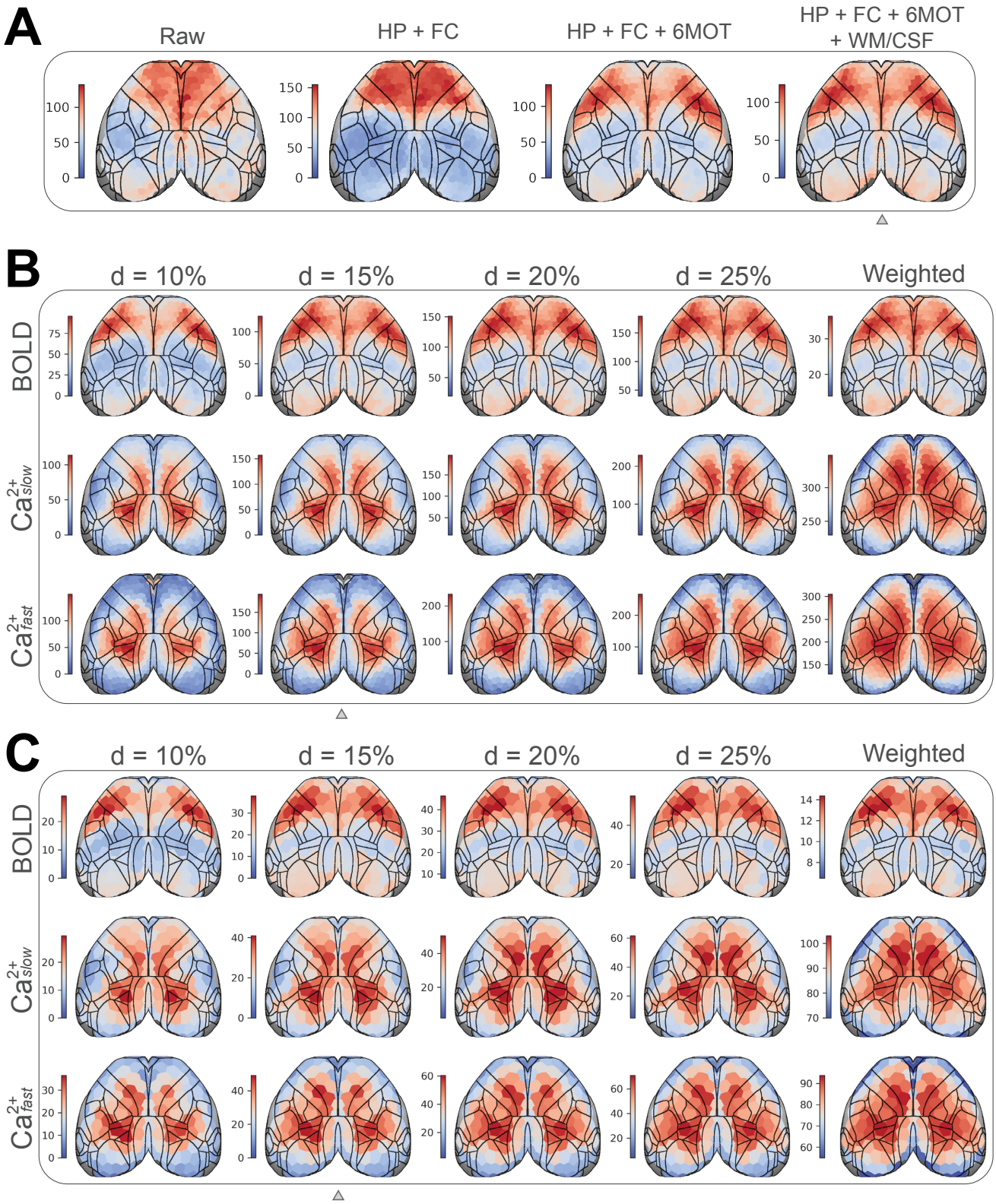

Figure S7: Dependence of degree centrality to data processing steps. **(A)** Spatial pattern of average degree depends on BOLD preprocessing steps. Raw, no confound regression; HP, 0.01 Hz high-pass; FC, frame censoring; 6MOT, motion regression (6 parameters); WM/CSF, average white matter and ventricles signal regressed out (this combination of processing steps was used in the main paper). **(B)** Degree patterns are robust to the choice of edge filtering threshold. Difference thresholds correspond to different scales, but the spatial patterns remain relatively similar. **(C)** Similar to B but for the coarse parcellation. Small triangles show that $d = 15\%$ was used in the main paper. See also Figure 6.